

The effects of plate interface rheology on subduction kinematics and dynamics

Whitney M. Behr¹, Adam F. Holt², Thorsten W. Becker^{3,4,5} and Claudio Faccenna^{6,7}

¹Geological Institute, Department of Earth Sciences, ETH Zurich, Sonneggstrasse 5, 8092 Zurich, Switzerland. E-mail: wbehr@ethz.ch

²Rosenstiel School of Marine and Atmospheric Science, University of Miami, 4600 Rickenbacker Causeway Miami, FL 33149-1031, USA

³Institute for Geophysics, Jackson School of Geosciences, The University of Texas at Austin, J.J. Pickle Research Campus, Bldg. 196 10100 Burnet Road, Austin, TX 78758-4445, USA

⁴Department of Geological Sciences, Jackson School of Geosciences, The University of Texas at Austin, 2275 Speedway Stop C9000, Austin, TX 78712-1722, USA

⁵Oden Institute for Computational Engineering and Sciences, The University of Texas at Austin, 201 E. 24th Street, Austin, Texas 78712-1229, USA

⁶Dipartimento Scienze, Laboratory of Experimental Tectonics, University of Roma Tre, L.S.L. Murialdo 1, Roma 00146, Italy

⁷Helmholtz Centre Potsdam GFZ, German Research Centre for Geosciences Potsdam (Germany), Telegrafenberg D-14473 Potsdam, Germany

Accepted 2022 February 19. Received 2022 February 13; in original form 2021 September 22

SUMMARY

Tectonic plate motions predominantly result from a balance between the potential energy change of the subducting slab and viscous dissipation in the mantle, bending lithosphere and slab–upper plate interface. A wide range of observations from active subduction zones and exhumed rocks suggest that subduction interface shear zone rheology is sensitive to the composition of subducting crustal material—for example, sediments versus mafic igneous oceanic crust. Here we use 2-D numerical models of dynamically consistent subduction to systematically investigate how subduction interface viscosity influences large-scale subduction kinematics and dynamics. Our model consists of an oceanic slab subducting beneath an overriding continental plate. The slab includes an oceanic crustal/weak layer that controls the rheology of the interface. We implement a range of slab and interface strengths and explore how the kinematics respond for an initial upper mantle slab stage, and subsequent quasi-steady-state ponding near a viscosity jump at the 660-km-discontinuity. If material properties are suitably averaged, our results confirm the effect of interface strength on plate motions as based on simplified viscous dissipation analysis: a ~ 2 order of magnitude increase in interface viscosity can decrease convergence speeds by ~ 1 order of magnitude. However, the full dynamic solutions show a range of interesting behaviour including an interplay between interface strength and overriding plate topography and an end-member weak interface-weak slab case that results in slab break-off/tearing. Additionally, for models with a spatially limited, weak sediment strip embedded in regular interface material, as might be expected for the subduction of different types of oceanic materials through Earth's history, the transient response of enhanced rollback and subduction velocity is different for strong and weak slabs. Our work substantiates earlier suggestions as to the importance of the plate interface, and expands the range of quantifiable links between plate reorganizations, the nature of the incoming and overriding plate and the potential geological record.

Key words: Fault zone rheology; Rheology and friction of fault zones; Dynamics of lithosphere and mantle; Rheology: crust and lithosphere; Subduction zone processes.

1 INTRODUCTION

The subduction interface is a shear zone of varying thickness that defines the boundary between a subducting slab and the overriding lithosphere. The thermal and mechanical properties of these shear zones affect a wide range of tectonic processes such as the transport

of volatiles from Earth's surface to its deep interior (e.g. Kerrick & Connolly 2001; Wada *et al.* 2008; Bebout 2013), the growth of continents and topography (e.g. Von Huene & Scholl 1991; Foley *et al.* 2002; Bassett & Watts 2015) and the amounts and rates of return flow of subducted material back to the surface (e.g. Gerya *et al.* 2002; Burov *et al.* 2014).

Observations from modern and exhumed subduction complexes suggest that subduction interfaces exhibit quite different characteristics from place to place and over geological time. Modern subduction zones, for example, show a wide variation in the types of materials entering the trench, with some blanketed by sediments sourced from local seafloor depocentres and/or nearby terrestrial landmasses (Von Huene & Scholl 1991; Rea & Ruff 1996; Clift 2017); and others that are sediment-poor and dominated by oceanic crustal seamounts or other forms of seafloor topography (Cloos 1993; Abercrombie *et al.* 2001; Laursen *et al.* 2002). These differences appear to produce variations in the state of stress, fluid pressure and seismic coupling along the subduction interface within and around the seismogenic layer (Cloos 1992; Scholz & Small 1997; Gulick *et al.* 2011; Heuret *et al.* 2012; Barnes *et al.* 2020), which suggests that differences in the types of material delivered to the trench are correlated with differences in interface rheological properties. This notion is also supported by laboratory friction experiments on materials collected from seafloor drilling sites (Kurzwski *et al.* 2018; Boulton *et al.* 2019; Seyler *et al.* 2020), as well as geological observations from accretionary complexes that are exposed onshore (Fagereng & Sibson 2010; Kitamura & Kimura 2012; Clarke *et al.* 2018; Phillips *et al.* 2020; Braden & Behr 2021).

Data from ancient exhumed subduction complexes furthermore suggest that the heterogeneity we see in materials entering trenches may also persist with progressive subduction along the interface to significant depth. Remnants of subduction interface shear zones exhumed from below seismogenic depths, for example, can show quite variable protolith compositions along strike and/or at different structural levels (see the compilation of fossil subduction interfaces in Agard *et al.* 2018). These commonly range from metasedimentary rocks (representing sediment cover), to metabasalts and metagabbros (representing mafic oceanic crust), to serpentinites and peridotites (potentially representing subducted oceanic mantle). Where these different protolith rock types are juxtaposed, they exhibit geological evidence for significant variations in their rheological properties, such as boudin–matrix relationships, sharp strain gradients or differences in deformation mode (brittle versus ductile) or mechanism (diffusion versus dislocation creep, Stöckhert *et al.* 1999; Angiboust *et al.* 2011; Grigull *et al.* 2012; Kotowski & Behr 2019; Tewksbury–Christle *et al.* 2021). Seismic images of the deep forearc region also suggest that the thicknesses and mechanical properties of the deep subduction interface vary among different subduction zones or within individual subduction zones along-strike (Nedimović *et al.* 2003; Han *et al.* 2017; Audet & Schaeffer 2018; Calvert *et al.* 2020; Delph *et al.* 2021; Tewksbury–Christle & Behr 2021).

Several workers have used these observations of mechanical contrast of subducting materials on both the shallow and deep interface to hypothesize that subducting sediments have the propensity to act as a lubricant to interplate sliding. Cloos (1985), for example, first suggested that sediment-dominated melange could define a narrow, low viscosity channel between the downgoing and overriding plates. Lamb & Davis (2003) raised the prospect of sediment lubrication as an explanation for temporal variations in upper plate topography in the Andes, based on the inference that sediments increase megathrust pore fluid pressures and decrease friction, and thereby control coupling between the slab and the upper plate. Recently, Behr & Becker (2018) demonstrated that viscous sections of subduction interfaces should also be sensitive to sediment subduction because metasedimentary protoliths are two to three orders of magnitude weaker than mafic protoliths based on experimentally derived viscous creep laws (e.g. Jin *et al.* 2001; Hirth *et al.* 2001; Zhang *et al.* 2006; Tokle *et al.* 2019). Behr & Becker (2018) used a simplified

energy balance for plate speeds based on constant geometry, simplified subduction from Conrad & Hager (1999) to show that interface viscosity variations could significantly influence plate convergence rates. Sobolev & Brown (2019) invoked this mechanism to suggest that sedimentation at continental margins, driven by erosion during global deglaciation events, could explain the onset of fast subduction rates characteristic of modern plate tectonics.

The hypothesis that interface effective rheology is sensitive to sediment subduction, and by corollary that sediment subduction may influence large-scale subduction dynamics is intriguing because it implies a potential feedback between the processes that control seafloor sedimentation (e.g. climate-driven terrestrial supply and/or organically driven seafloor deposition) and tectonic plate motions (Lamb & Davis 2003; Behr & Becker 2018; Sobolev & Brown 2019; Chen *et al.* 2022). However, the impact of plate interface viscosity on subduction dynamics is relatively underexplored in dynamically consistent numerical subduction models and, in particular, the impact of interface strength on near-surface subduction properties like topography and upper plate stress is unclear. Some recent time-dependent modelling studies show that interface viscosity can indeed impact slab dynamics significantly; particularly slab rollback rates, plate velocities and slab interactions with the viscosity jump at the 660-km-seismic discontinuity (Androvičová *et al.* 2013; Čížková & Bina 2013; Ratnaswamy *et al.* 2015; Pokorný *et al.* 2021). More typically, however, the interface is implemented as a constant viscosity region, or a constant shear stress fault, in large-scale subduction simulations and is set to be weak enough to permit steady-state subduction at Earth-like convergence rates (King & Hager 1990; Zhong & Gurnis 1995a; Billen & Gurnis 2001). The formulation by Conrad & Hager (1999), utilized in Behr & Becker (2018), does not take into account the time-dependent evolution of the subducting slab or the potential influence of power law creep rheologies in the mantle, nor did that study permit the examination of different kinematic components of the subduction system (e.g. subducting plate velocity, overriding plate retreat rate and convergence rates). Thus, several open questions remain, including the following:

- (i) How does interface viscosity influence subduction kinematics, including both the early transient (pre-660) and later, ~steady-state (post-660) rates of slab sinking, overriding plate retreat and plate convergence?
- (ii) How and over what timescales do slab kinematics respond to sudden changes in interface viscosity?
- (iii) How do variations in interface viscosity affect overriding plate stress state and topography?
- (iv) What is the relative importance of oceanic crust and overriding plate buoyancy in subduction plate speeds compared to interface viscosity?

In this paper, we address these questions using fully dynamic 2-D numerical models of subduction of oceanic lithosphere beneath a continental overriding plate. We systematically investigate slab kinematics and morphology for varying slab strengths, interface viscosities, and density structures and discuss the implications for linkages between subduction dynamics and surface processes.

2 MODELLING APPROACH

2.1 Model framework

We use the finite element code ASPECT (v. 2.1.0; Kronbichler *et al.* 2012; Heister *et al.* 2017) to solve the equations that govern

convection in an incompressible viscous fluid with negligible inertia and no internal heating. This includes the conservation of mass:

$$\nabla \cdot \mathbf{v} = 0 \quad (1)$$

momentum:

$$-\nabla \cdot (2\eta\dot{\epsilon}) + \nabla p = \rho \mathbf{g} \quad (2)$$

and energy:

$$\rho C_p \left(\frac{\partial T}{\partial t} + \mathbf{v} \cdot \nabla T \right) - k \nabla^2 T = 0, \quad (3)$$

where \mathbf{v} is velocity, $\dot{\epsilon}$ the strain-rate tensor, η viscosity, p pressure, ρ density, \mathbf{g} gravitational acceleration, C_p specific heat capacity, T temperature and k thermal conductivity Table 1.

Our general set-up follows that of, for example, Holt *et al.* (2015) in that a compositionally controlled, crustal layer with properties that can be varied between models allows for dynamic subduction within a thermochemical convection system with a freely moving subducting and overriding plate. The composition is advected as a compositional field. The details of the rheology and density structure are provided below, but our model set-up is similar to that outlined in Holt & Condit (2021) with a domain size that is 2900 km deep (whole mantle) and 11 600 km wide (Fig. 1). The model is initiated with two flat-lying lithospheric plates of different ages. The subducting plate is 6000-km-long, 80 Ma old, and is placed next to a 2500-km-long, 60 Ma old overriding plate. The overriding plate is compositionally buoyant and stiff relative to the subducting plate so as to approximate a continental-affinity upper plate. Both plates are bounded on the outer model margins by ridge segments and are separated from each other by a thin crustal layer (discussed further below). The subducting plate is pre-bent with a radius of curvature of 250 km and extends to an initial depth of 200 km. All model mechanical boundaries are free slip.

Our models are self-consistent in that all dynamics and deformation are driven by internally generated forces and without imposed kinematics. However, it should be noted that this does not necessarily mean that they are regionally realistic. For example, our models are 2-D, which means that they are most applicable in the centre of wide slabs. Moreover, regional tectonics on Earth may be affected by far-field plate forces, for example, and along-strike variations in various slab/trench/upper plate properties; those are not included in our study in order to be able to isolate the local dynamics and effects of rheology.

2.2 Temperature and density structure

The two lithospheric plates are defined using half-space cooling profiles for lithosphere of 80 (subducting plate) and 60 Ma (overriding plate), a thermal diffusivity of $10^{-6} \text{ m}^2 \text{ s}^{-1}$ and a mantle potential temperature of 1300 °C. Density is temperature dependent with different reference densities for the background material (oceanic lithosphere and sublithosphere mantle), the overriding plate lithosphere and the oceanic crust. In the reference case, the crust and overriding plate material (both tracked by separate compositional fields) have densities that are reduced relative to that of the oceanic lithosphere/mantle (3175 kg m^{-3} reference density, relative to 3300 kg m^{-3}). This is to approximate the lower density of basaltic crust, and to ensure the upper plate is positively buoyant and hence remains at the surface. In the upper plate, this compositional component extends to an initial depth of 100 km.

2.3 Rheology

2.3.1 Asthenosphere and lower mantle.

The rheology of the mantle in our models is governed by a composite creep law with diffusion creep, dislocation creep and plastic yielding in order to capture the first-order controls on subduction-induced flow and deformation (e.g. Billen & Hirth 2005; Garel *et al.* 2014).

The dislocation and diffusion creep laws are parametrized as:

$$\eta_{\text{diff/dist}} = A^{-\frac{1}{n}} \dot{\epsilon}_{II}^{\frac{1-n}{n}} \exp\left(\frac{E + PV}{nRT}\right), \quad (4)$$

where η is the composite viscosity, A is a pre-factor, $\dot{\epsilon}_{II}$ is the second invariant of the strain rate tensor, n is the stress exponent, R is the gas constant, P is the lithostatic pressure and T is the temperature. The stress exponents (n) (dislocation creep = 3.5, diffusion creep = 1), activation volumes (V) and energies (E) are consistent with the range of values derived from laboratory experiments on wet olivine (Hirth & Kohlstedt 2004). Despite assuming incompressibility in our models, we add a $0.3 \text{ }^\circ\text{C km}^{-1}$ adiabatic temperature gradient to the temperature used in eq. (4). The diffusion and dislocation creep pre-factors are set to give $\eta_{\text{diff}} = \eta_{\text{dist}} = 5 \times 10^{20} \text{ Pa s}$ at a transition strain rate of $5 \times 10^{-5} \text{ s}^{-1}$ and depth of 330 km (*cf.* Billen & Hirth 2005). The lower mantle is more viscous than the upper mantle and is set to only deform via diffusion creep. The lower mantle diffusion creep pre-factor is computed to produce an upper-to-lower mantle diffusion creep viscosity increase of factor 20. This factor of 20 increase in viscosity allows us to test the effect of a reduction in slab sinking rates and the resulting ‘anchoring’, similar to numerous prior studies. While exact values for and the depth of such an increase are unclear (e.g. King & Masters 1992), geoid and slab sinking rate studies indicate that the lower mantle has a higher viscosity than the upper mantle (e.g. Hager 1984; Ricard *et al.* 1993).

The equivalent plastic ‘viscosity’ is defined as:

$$\eta_{\text{yield}} = \frac{\min(\tau_{\text{yield}}, 0.5 \text{ GPa})}{2\dot{\epsilon}_{II}} \quad (5)$$

and τ_{yield} is approximated by a Coulomb friction criterion for optimally oriented faults:

$$\tau_{\text{yield}} = (a\sigma_n + b)\lambda \quad (6)$$

in which a is the friction coefficient (0.6), b is the cohesion (60 MPa), λ is a pore fluid factor defined as $\lambda = 1 - \frac{P_{\text{fluid}}}{P_{\text{rock}}} = 0.15$ and σ_n is assumed to equal the lithostatic pressure P . This value of λ results in significant plastic weakening, yet does not weaken the trench region completely, and is comparable to that required to produce coherent downwellings/slabs in previous convection/subduction modelling studies [e.g. Enns *et al.* (2005): 0.1, Moresi & Solomatov (1998): 0.03–0.13].

The effective model viscosity is then calculated as:

$$\eta_{\text{eff}} = \left(\frac{1}{\eta_{\text{diff}}} + \frac{1}{\eta_{\text{dist}}} + \frac{1}{\eta_{\text{yield}}} \right)^{-1} \quad (7)$$

and is capped with upper and lower limits of, respectively, 2.5×10^{18} and $2.5 \times 10^{23} \text{ Pa s}$ in the reference model set-up. In regions without plastic yielding, our rheological parameters produce a reference viscosity of $2.5 \times 10^{20} \text{ Pa s}$ (at $\dot{\epsilon}_{II} = 5 \times 10^{-5} \text{ s}^{-1}$, depth = 330 km).

Table 1. Model parameters.

Quantity	Symbol	Units	Value(s)
Temperature/density			
Surface temperature	T_s	K	273
Potential temperature	T_m	K	1573
Adiabatic temperature gradient	$d_z T$	K km ⁻¹	0.3
Reference density (slab/mantle)	ρ_0	kg m ⁻³	3300
Reference density (crust/overriding plate)	ρ_C	kg m ⁻³	3175
Thermal expansion coefficient	α	K ⁻¹	3×10^{-5}
Thermal diffusivity	κ	m ² s ⁻¹	10^{-6}
Lithosphere properties			
Subducting plate age	t_{SP}	Myr	80
Subducting plate viscosity (core)	η_{core}	Pa s	2.5×10^{24}
Subducting plate viscosity (non-core)	η_{SP}	Pa s	2.5×10^{22} ; 2.5×10^{23}
Overriding plate age	t_{OP}	Myr	60; 120
Overriding plate viscosity	η_{OP}	Pa s	2.5×10^{24}
Overriding plate compositional thickness	h_{OP}	km	100; 150
Crust viscosity	η_{crust}	Pa s	2.5×10^{18} ; 10^{19} ; 10^{20} ; 10^{21}
Dislocation creep (upper mantle)			
Activation energy	E	kJ mol ⁻¹	540
Activation volume	V	cm ³ mol ⁻¹	12
Prefactor	A	Pa ⁻ⁿ s ⁻¹	8.5×10^{-15}
Exponent	n	–	3.5
Diffusion creep (upper and lower mantle)			
Activation energy	E	kJ mol ⁻¹	300 (UM, LM)
Activation volume	V	cm ³ mol ⁻¹	4 (UM), 2.5 (LM)
Prefactor	A	Pa ⁻¹ s ⁻¹	10^{-10} (UM); 5.8×10^{-13} (LM)
Exponent	n	–	1
Plastic yielding			
Friction coefficient	a	–	0.6
Cohesion	b	MPa	60
Pore fluid factor	λ	–	0.1
Maximum yield stress	τ_{max}	MPa	500

2.3.2 Lithospheric mantle and crust

Aside from where plastic yielding is activated, in the bending region of the slab, this upper viscosity limit (2.5×10^{23} Pa s) dictates the lithospheric strength. In the overriding plate, we increase this upper limit to by an order of magnitude (2.5×10^{24} Pa s) to mimic a stiff overriding plate. As detailed in Section 2.5, we also test the effects of a strong slab core (cf. Capitanio *et al.* 2007; Buffett & Becker 2012) by increasing the upper viscosity limit within a 12.5-km-thick layer in the centre of the subducting lithosphere. Like the crust and overriding plate, this slab core region is tracked using a distinct compositional field. The crust is a 7.5-km-thick oceanic crustal layer (in some cases referred to as an ‘oceanic weak layer’), which is placed along the curved slab top and is prescribed a constant viscosity (Fig. 1).

2.4 Numerical parameters

Adaptive mesh refinement (AMR) is set to occur for the $Q_2 - P_1$ finite elements associated with high viscosity gradients, high temperature, and/or non-zero compositions (Bangerth *et al.* 2018). This enables us to highly resolve our (compositional) crust while also capturing large-scale mantle flow and slab dynamics. In models with a slab core, and hence another compositional field, we also refine the mesh within this core. The AMR parameters produce a maximum level of refinement corresponding to 2.8-km-wide finite elements (in the crust and core). This maximum refinement corresponds to three levels of adaptive mesh refinement on top of seven

levels of globally uniform refinement (Bangerth *et al.* 2018). See Holt & Condit (2021) for numerical accuracy and mesh resolution tests for comparable model set-ups.

2.5 Model analysis and varied parameters

For each model run, we quantitatively track: (i) the slab kinematics, including subducting plate velocity (V_{sp}), overriding plate velocity (V_{op}), and convergence velocity (V_c); (ii) slab dip (extracted at 200 km depth); (iii) viscosity, stress and temperature distributions and (iv) topographic evolution. We compute surface topography from the vertical normal stress (σ_{xx}) at the free slip upper boundary. This assumes the corresponding free surface, with zero normal stress, would deflect according to this normal stress (e.g. Zhong & Gurnis 1994). We also qualitatively examine the slab morphology near the 660-km-discontinuity and the interface shear zone thickness and geometry near the trench. We vary the following parameters between different model runs:

(i) *Slab average strength.* We explore three different effective slab strengths. The strongest slab case is implemented with a high-viscosity (unyielding) core in the centre of the slab (2.5×10^{24} Pa s) and relatively high pre-yield viscosity elsewhere in the lithosphere (2.5×10^{23} Pa s); whereas the other two have no slab core and variable pre-yield viscosities (2.5×10^{23} Pa s, 2.5×10^{22} Pa s). In subsequent sections, we refer to the three slab types as strong, intermediate and weak.

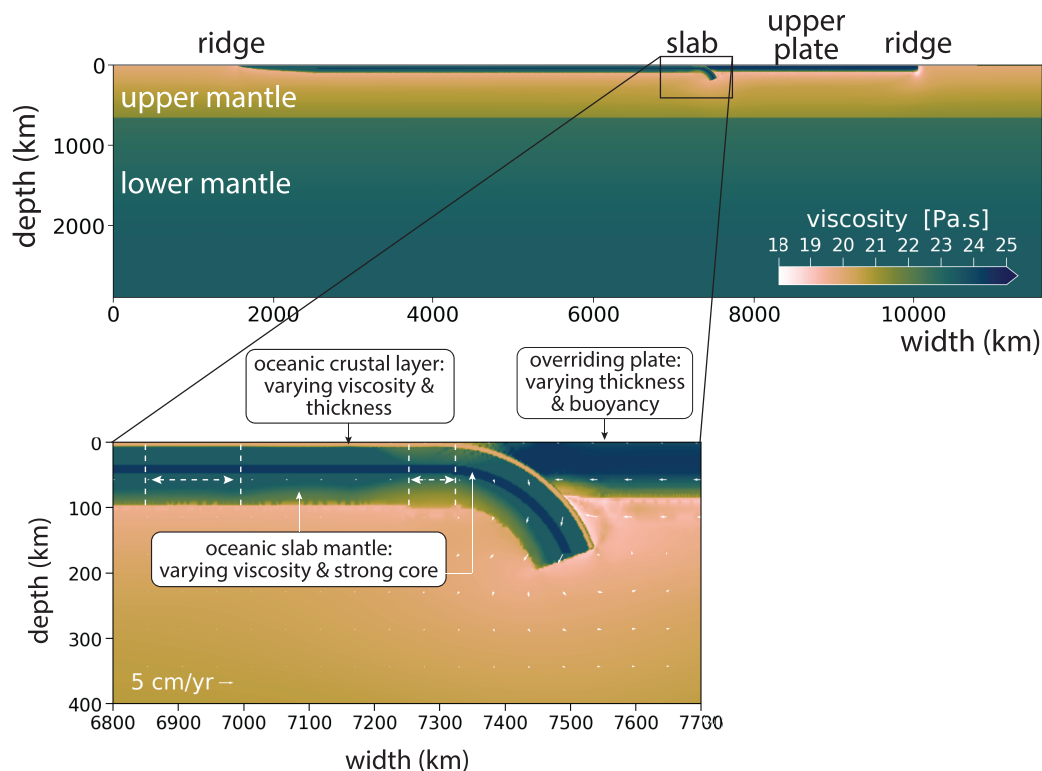


Figure 1. Model set-up with initial viscosity field and zoomed in view of the subduction interface region. White text boxes and arrows point to parts of the model that are varied (see text for details). Dashed white lines show the regions over which slab viscosity is averaged both within and away from the bending region.

(ii) *Oceanic crustal/weak layer viscosity and thickness.* The oceanic crustal/weak layer viscosity is varied from 2.5×10^{18} to 10^{21} Pa s. In some models the whole crustal layer is assigned the same viscosity, whereas in others a lower viscosity section is implemented as a 500-km-wide low-viscosity strip embedded within higher viscosity crust. Physically, the low viscosity crustal/weak layer could correspond to, for example, layers of particularly weak sediments (e.g. Vrolijk 1990; Tobin & Saffer 2009), exhumed seafloor serpentinite (e.g. Minshull 2009; Guillot *et al.* 2015), or patches of exceptionally altered/weak oceanic crustal igneous rock (e.g. Braden & Behr 2021). We also vary the thickness of the oceanic weak layer from 7.5 to 10 to 12.5 km in some models.

(iii) *Overriding plate thickness and density.* Motivated by the occurrence of different upper plate tectonic histories (e.g. cratonic versus thinned continental lithosphere versus oceanic), we explore the impact of variable upper plate thickness/density. In addition to the reference parametrization (60 Ma upper plate with 100-km-thick compositionally buoyant/stiff portion), we consider a thickened upper plate model (120 Ma age, 150 km compositional thickness), and a 60 Ma upper plate case with the compositionally buoyant/stiff component eliminated.

(iv) *Oceanic crustal density.* While most models contain crusts and overriding plates that are lighter ($\rho_0 = 3175 \text{ kg m}^{-3}$) than the surrounding material ($\rho_0 = 3300 \text{ kg m}^{-3}$), we also examine the effects of removing this computational buoyancy from both elements. This is to ensure first-order model behaviour holds in the presence of eclogitized oceanic crust and/or oceanic upper plates.

(v) *Crustal cut-off depth.* In all models, we remove the crust at a certain depth in the mantle. In most of our models, we gradually taper the weak and buoyant crust from full thickness at 200 km

depth to zero thickness at 300 km depth in order to reduce stress discontinuities. Because the persistence of weak material to mid-mantle depths creates an overly thickened cold forearc region (e.g. Kincaid & Sacks 1997), which conflicts with petrological and heat flow evidence for a warm mantle wedge (e.g. Furukawa 1993; Wada & Wang 2009) we test the effect of discretely cutting the crust off at a shallower, 100 km depth [which eliminates this issue in dynamic models: e.g. Holt & Condit (2021)].

3 RESULTS

3.1 Effect of varying slab strength

Fig. 2 illustrates the effects of variable slab strength for uniform, 10^{20} Pa s plate interface strength. Plotted are four time steps for the strongest and weakest slab end-members (Figs 2a and b) along with the subducting plate, overriding plate, and convergence velocities for the three slab types (Figs 2c–e) implemented here. The general dynamics of these self-consistent subduction models are comparable to earlier work (e.g. Garel *et al.* 2014; Holt & Becker 2016) and can be considered as ‘typical’ of such self-consistent upper mantle scenarios with diffusion/dislocation creep viscoplastic rheologies.

All three slab types show plastic yielding in the bending region at the start of model run (*cf.* Enns *et al.* 2005; Stegman *et al.* 2006). Fig. 3 shows the computed average (geometric mean) viscosity both away from and near the bending region of the plate (see Fig. 1 for averaging locations) for the three slab strength categories. The average viscosity in the bending region for the weak and strong slab end-members differ by slightly more than one order of magnitude. Our effective slab viscosities are a few orders of magnitude

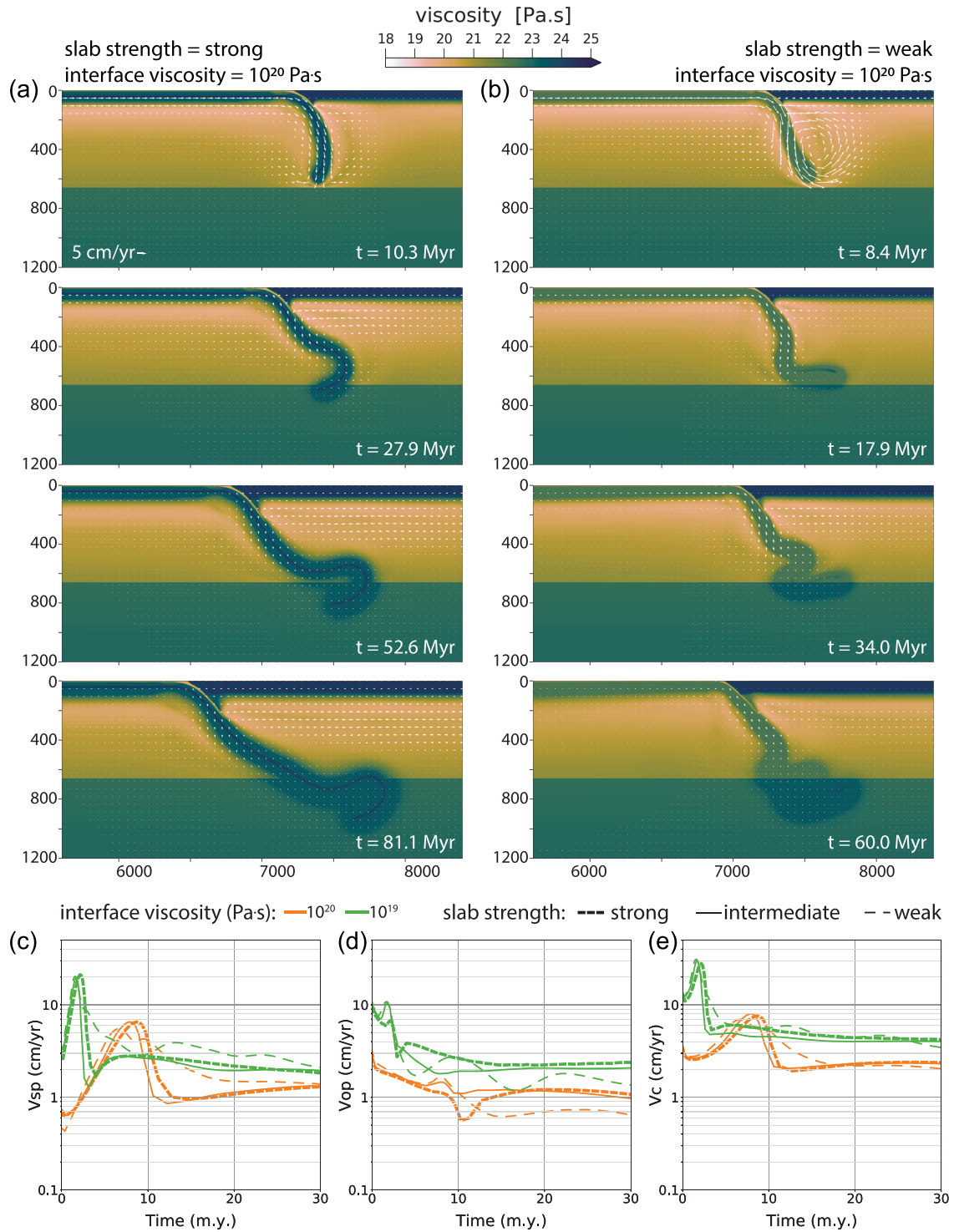


Figure 2. Model snapshots and kinematics for end-member slab strengths. (a and b) Pre- and post-660 snapshots of model runs with a strong slab (a) and a weak slab (b) for the same subduction interface strength. (c–e) Kinematics of models for various slab strengths (strong, intermediate and weak) and two different interface viscosities.

larger than the background asthenosphere; this is lower than what would be expected from application of laboratory constraints for olivine diffusion and dislocation creep. However, such moderate strength slabs are consistent with a range of observations including: low elastic thickness at the trench (Billen & Gurnis 2005); large strain-rates within slabs (Holt 1995); tomographically imaged

slab morphologies, which indicate low viscosity fluid deformation, likely accommodated by plastic yielding (e.g. Čížková *et al.* 2002; Garel *et al.* 2014); and more indirect inferences from plate driving force and slab dynamics considerations (e.g. Funicello *et al.* 2008; Wu *et al.* 2008; Buffett & Becker 2012, *cf.* Billen 2008; Becker & Faccenna 2009).

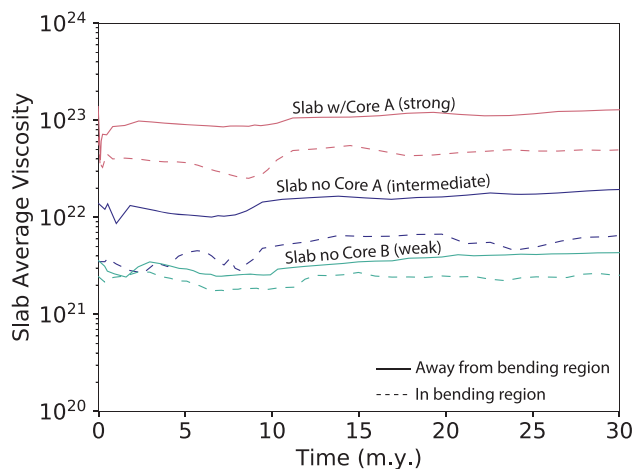


Figure 3. Slab average viscosities over time away from the bending region (solid lines) and within the bending region (dashed lines) for the four slab types implemented in this model suite. See Fig. 2 for locations of averaging regions.

All three models show an early transient peak in convergence velocities driven primarily by rapid subducting plate motion (V_{sp}) as the slab sinks rapidly through the relatively weak upper mantle (Fig. 2). Upon approaching the 660 km viscosity increase, the sinking velocity for the strong and intermediate slab strength cases decelerates rapidly, whereas deceleration is slower for the weaker slab due to more prolonged slab stalling in the transition zone. At the same time, however, the weakest slab exhibits lower overriding plate velocities post-660. Because deformation in the overriding plate is negligible in all model runs (due to it being compositionally stiff), V_{op} is approximately equivalent to the rate of trench retreat/slab rollback. Despite small V_{sp} and V_{op} differences between the weakest slab case and the other slab strengths, all three slab strengths exhibit similar post-660 convergence velocities after ~ 15 Myr. Similar kinematic patterns are observed for the case of a weaker (10^{19} Pa s) subduction interface and equivalently variable slab strengths (green lines, Figs 2c–e).

These results suggest that slab strength, within the moderate ranges of contrast to the asthenosphere (*cf.* Billen 2008; Becker & Faccenna 2009) that we explore here, does not substantially affect convergence velocities, as expected (Conrad & Hager 1999). Figs 2(a) and (b), however, agrees with previous modelling studies that show slab strength has a strong effect on the morphology of the slab when it reaches an upper-to-lower mantle viscosity increase; the strong slab exhibits early buckling, followed by ponding, whereas the weaker slab shows much tighter-wavelength folding and continuous sinking through the transition zone with limited ponding (*cf.* Davies 1995; Christensen 1996; Ribe *et al.* 2007; Billen 2008; Garel *et al.* 2014).

3.2 Effects of varying interface viscosity

Fig. 4 shows model snapshots and kinematics for interfaces varying over four orders of magnitude for a single (strong) slab strength. For the strongest interface case (10^{21} Pa s), subduction is extremely slow with convergence rates less than ~ 5 mm yr $^{-1}$. This low Peclet number setting results in substantial thermal diffusion of the slab within the upper mantle prior to it reaching the 660-km-discontinuity, which results in its viscosity structure being dominated by the stiff,

compositional core (Fig. 4a). Thus an end-member emerges that represents effective subduction stalling, so in subsequent discussions, we focus on the three lower viscosity interface cases (strong = 10^{20} Pa s, weak = 10^{19} Pa s, very weak = 2.5×10^{18} Pa s).

As in the variable slab strength models discussed in Section 3.1, all three models first show an early increase in convergence velocity (V_c) associated primarily with rapid slab sinking through the relatively weak upper mantle (Fig. 4e). The magnitude and timescale of this transient phase of fast subducting plate velocities and plate convergence scales with interface viscosity, with the weakest interface exhibiting convergence rates of up to 13 cm yr $^{-1}$ over a 2 Myr time interval, and the moderately strong interface peaking at ~ 7 cm yr $^{-1}$ over a ~ 7 Myr pulse (Fig. 4g). Overriding plate velocity (V_{op}), which is approximately equal to trench velocity, also scales with interface viscosity, with fastest trench retreat for the very weak interface case (Fig. 4f). In addition to being in direct response to the viscosity reduction (and hence shear stress reduction) at the deep plate interface, subducting plate velocities within the weak and very weak interface models are further enhanced by local decreases in upper mantle viscosity around the slab due to the dominance of dislocation creep within these high strain rate regions (*cf.* Figs 4c and d).

Upon reaching the 660, V_{sp} immediately decreases due to the increase of mantle viscosity for all three interface cases, whereas V_{op} reaches an approximately constant velocity, with faster rates of trench retreat for the weaker interfaces, after a steady decrease during the pre-660 phase. With time, the fast rollback associated with the two weakest interfaces causes the slab dip to shallow resulting in a repartitioning of the slab pull force. The strong interface case, by contrast, exhibits slower overriding plate retreat and retains a steeper dip and an approximately constant subducting plate velocity such that there is both more slab penetration through the 660 and, due to the low convergence rates, more accumulation of thermally thickened slab in the ~ 300 -km-thick region surrounding the viscosity increase. Post-660 convergence rates reach an approximate steady state for all models, with V_c remaining fastest for the very weak interface case and slowest for the strong interface case (Fig. 4g). The interface viscosity variations also result in differences in the morphology of the trench and interface shear zone itself after the slab reaches the 660. The fast rollback and shallower dip of the slab in the weak interface cases produces a longer and thicker interface shear zone.

In addition to exploring the effects of plate interface strength on the strong slab models (*i.e.* with a core), we also conducted equivalent tests for the other two, relatively weaker, slab strength cases. Fig. 5 summarizes V_{sp} , V_{op} and V_c computed both before (maximum) and after (time-average) the slab reaches the 660 for all model runs as a function of interface viscosity and colour-coded by slab strength. This shows that the first-order effects of varying plate interface strength on subduction kinematics hold for variable slab strengths, and that convergence velocities and related subduction kinematics both pre-and post-660 can vary by more than one order of magnitude depending on the strength of the interface (*cf.* Čížková & Bina 2013; čížková & Bina 2019). Interestingly, an additional behavioural end-member emerges here when both the slab and interface are set to the weakest end-member cases; this model exhibits slab break-off within 1 Myr of the model run, prior to the slab reaching the 660. That is, the combination of weak slab (low bending resistance) and weak interface (low mantle resistance) manifest as high slab pull transmission to the shallow slab and hence ‘plastic’ yielding throughout the entire lithosphere for our chosen yield stress parameters.

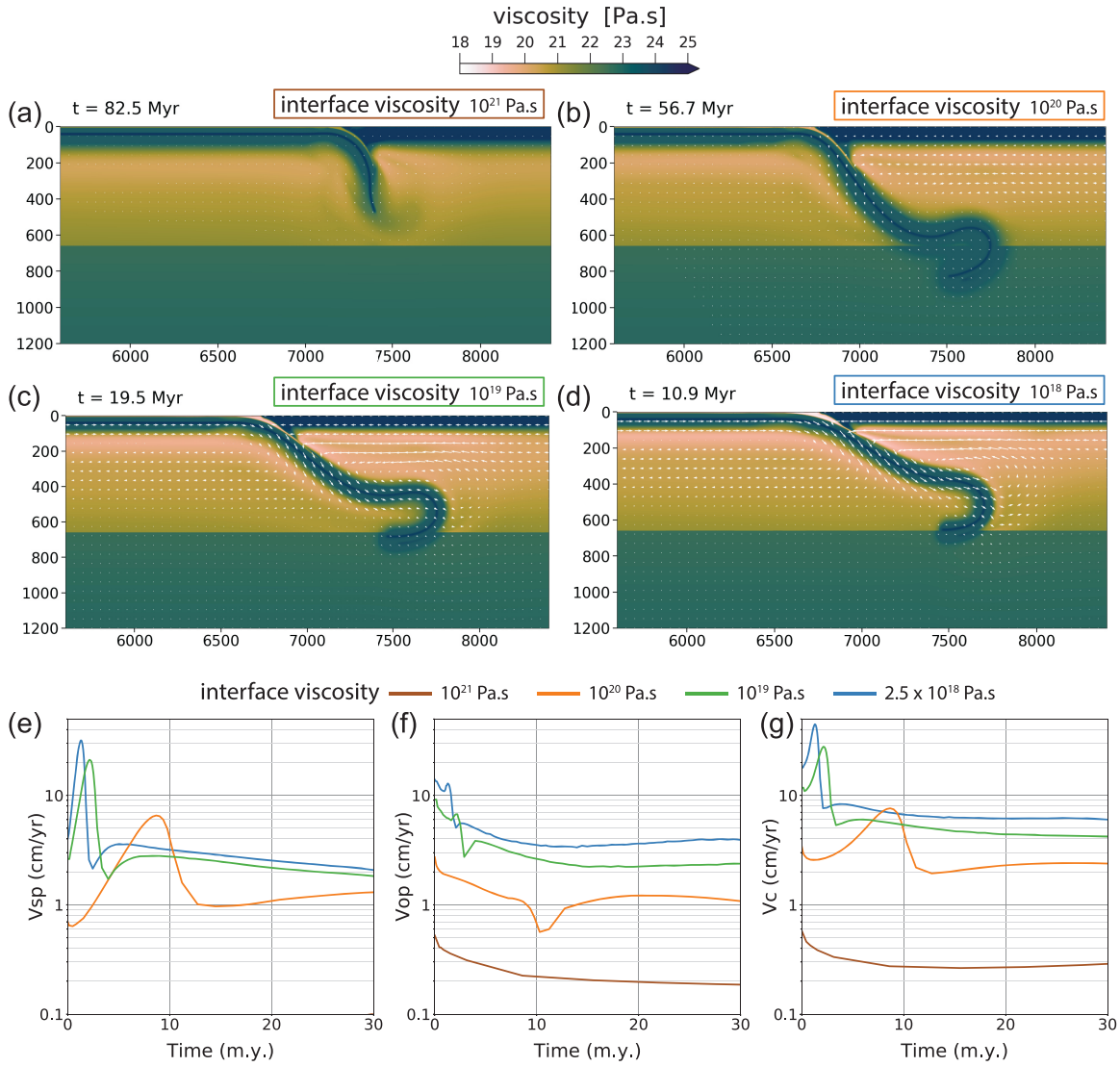


Figure 4. Effects of varying interface viscosity for a single (strong) slab strength. (a–d) Snapshots of the viscosity profile through models with different interface viscosity. (e–g) Kinematics of the models colour-coded by interface viscosity. (V_{sp} for the strongest interface viscosity is not shown in (e) because it is lower than 0.1 cm yr^{-1} .) See text for detailed description, and supporting information for videos of these model runs.

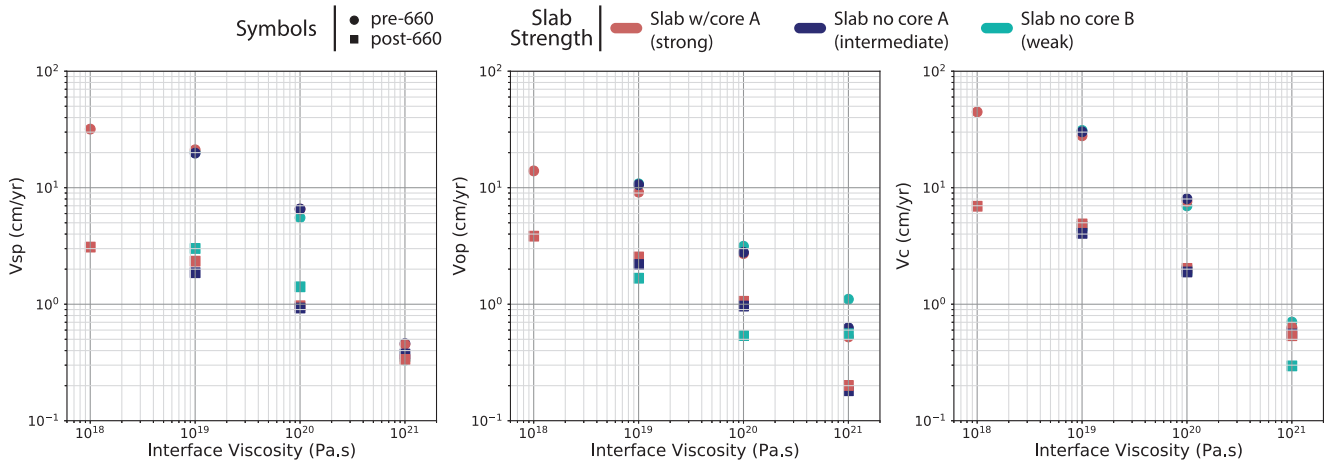


Figure 5. Summary plots of key parameters as a function of interface viscosity, colour-coded by slab strength, with symbols showing metrics computed prior to (circles) and after (squares) the slab reaches the 660. Pre-660 velocities plotted are maxima whereas post-660 velocities plotted are time-averages.

3.3 Kinematic response to transient changes in interface rheology

All previously described model runs had a constant viscosity assigned to the oceanic weak layer on top of the subducting slab. Here we examine the kinematic responses to a sudden change in interface viscosity. Fig. 6 shows the kinematic indicators for models in which the oceanic crustal layer exhibits a high viscosity (strong interface case = 10^{20} Pa s), except for the presence of a 500-km-long-strip in the centre of the downgoing plate (initially 500 km from the trench). Fig. 6 shows the results from two model cases, one in which the strip is weak (10^{19} Pa s) and the other in which the strip is very weak (2.5×10^{18} Pa s) relative to the ambient crust (10^{20} Pa s). In both models the strip enters the trench just after the slab begins to interact with the 660. The immediate response to the low viscosity strip in both model runs is an increase in slab rollback velocity ($\approx V_{op}$) and an associated increase in convergence rate. The pulse of fast rollback is then followed by a period of faster slab sinking for both model runs. For the weak strip tests conducted for slab strength set at the weak end-member, the peak in early V_{op} velocity (rollback) is closely spaced in time to the peak in subducting plate velocity (V_{sp} , *cf.* Fig. 6b). This produces a single pulse-like increase in convergence velocity, of about a factor of two over ~ 15 Myr, associated with the low viscosity strip subduction (Fig. 6h). Fig 6(b) shows that the peak convergence velocity achieved during weak strip subduction for the weak slab case reaches the same velocity as the uniformly weak interface model case. For the strong slab models with a weak strip, the behaviour is quite different. In these models the early slab rollback peak is distinctly separated in time from a later peak in slab sinking velocity (*cf.* Figs 6c and e). This results in a much broader-wavelength, lower-amplitude increase in convergence velocity, with V_c elevated by a factor of ~ 1.5 over 50–60 Myr. The peak convergence velocities for these models remain lower than for the equivalent, uniform weak interface models because the length of the low viscosity strip is insufficient to allow the subducting plate to accelerate to its maximum convergence velocity.

3.4 Effects on upper plate stresses and topography

We also examined how the strength of the interface affects upper plate stress regime and topography. The upper boundary of our models is free slip and so dynamic topography is calculated to be that which would support the vertical normal stresses produced at the surface (e.g. Zhong & Gurnis 1994). Fig. 7 shows the spatial distribution of topography and horizontal deviatoric stress across the trench for two interface models (strong versus very weak interface) and a strong slab, both before and after the slab reaches the 660. Prior to the slab reaching the 660, both models exhibit a topographic high seaward of the bending region of the slab that represents viscous flexure associated with slab bending (e.g. Zhong & Gurnis 1994; Cramer *et al.* 2017). Both also show an overall increase in topography across the trench region and into the upper plate, which is due to the isostatic effect of a relatively light overriding plate being juxtaposed against the dense subducting plate.

The two models show a distinctive difference in the near-trench/forearc region (< 200 km from the trench), however; the strong interface model shows compressional stresses (Fig. 7b) and a pronounced topographic low (*cf.* Billen & Gurnis 2001), whereas the weaker interface exhibits neutral to extensional stresses and continuously increasing topography from the trench to the upper

plate. This difference likely occurs for two reasons: (i) in the strong interface case, the slab and forearc are strongly coupled across the interface such that the slab more effectively pulls down on the upper plate; (ii) flow in the mantle wedge corner is more vigorous in the weak interface case (Fig. 7c) such that there is more of a contribution from dynamic pressure effects. After the slab reaches the 660, the forearc stresses remain mostly compressional in the strong interface case (Fig. 7e), but the stress magnitudes are lower due to slab stalling and hence reduced plate velocities; the associated local topographic low in the forearc is less pronounced (Fig. 7d, Chen *et al.* 2017). In the weak interface case, shallowing of the slab dip after the slab reaches the 660 (Fig. 7f) results in reduced viscous flexure such that the topographic profile is approximately flat across the trench (Fig. 7d).

3.5 Effects of buoyancy, overriding plate thickness, weak layer thickness and crustal cut-off variations

All models discussed thus far included a compositionally light oceanic crust and overriding plate ($\rho_0 = 3175 \text{ kg m}^{-3}$), relative to the subducting lithosphere ($\rho_0 = 3300 \text{ kg m}^{-3}$), a constant overriding plate compositional thickness (100 km), a constant subducting crust thickness, and crustal material that is gradually tapered out at depths beyond 200 km. In Fig. 8, we illustrate the effects of relaxing these assumptions on convergence velocities. The removal of the oceanic crust compositional buoyancy (i.e. setting $\rho_0 = 3300 \text{ kg m}^{-3}$, Fig. 8a) results in faster convergence rates both before and after the slab reaches the 660 than both the cases of just no overriding plate compositional buoyancy or both oceanic crust and overriding plate compositional buoyancy (i.e. the reference). However, the effects of such buoyancy changes are much smaller than the effects of changing interface viscosity. Fig. 8(b) shows the effect of varying upper plate thickness for different interface viscosity cases. For the weak interface case, the thicker overriding plate does result in slightly slower convergence velocities prior to the slab reaching the 660, but the difference is negligible once the slab reaches a steady state. For the strong interface case, the effect of a thicker upper plate is more substantial prior to the slab reaching the 660, influencing both the peak convergence velocity and the timescale over which the subduction initiates, but the difference is again negligible after the slab reaches the 660. Fig. 8(c) also shows that changing the crustal cut-off depth by 100 km has only relatively minor effects on the model kinematics. Fig. 8(d) shows the results of increasing the thickness of the oceanic crust from 7.5 km as in the reference model to 10 and 12.5 km. As expected, a thicker oceanic crust results in faster convergence rates at constant crustal viscosity both prior to and after the slab reaches the 660. The effect is small, however, compared to the effect of changing interface viscosity by one order of magnitude (8d).

4 DISCUSSION

4.1 Comparison to viscous dissipation analysis

Our results confirm that interface viscosity can strongly influence convergence velocities both prior to and after slab interaction with a viscosity jump at the 660-km-discontinuity, through a combination of both faster slab rollback and faster slab sinking (Fig. 5). This overall effect is consistent with the viscous dissipation balance

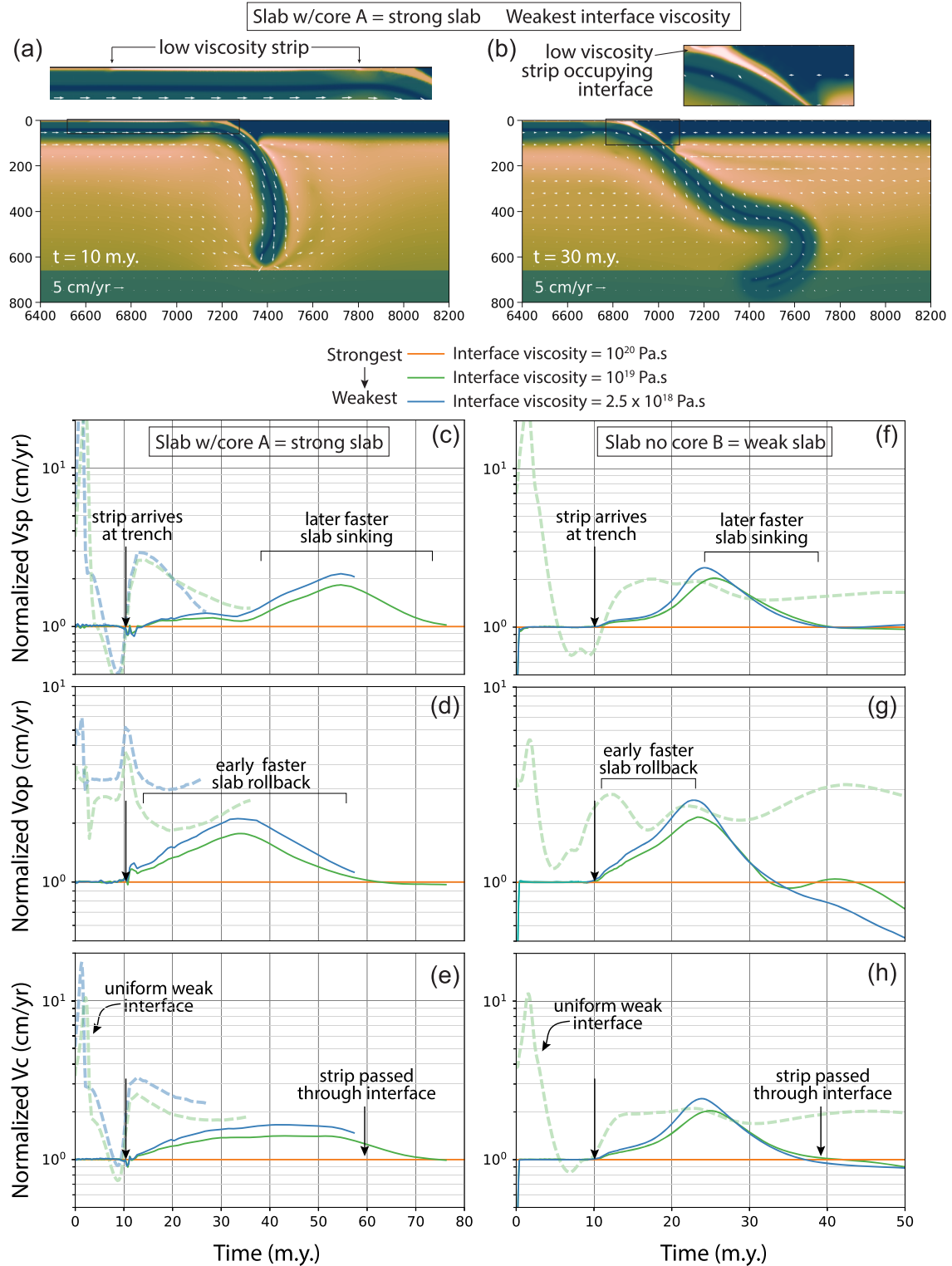


Figure 6. Kinematic response to a low viscosity crustal strip embedded in a higher viscosity surrounding crust. (a) Viscosity field snapshots of the low viscosity strip before and after it occupies the interface. (b) Velocity plots for strip models (blue and green solid curves) normalized to the constant-interface-viscosity case of 10^{20} Pa s (orange curves). The three kinematic parameters show increases associated with passage of the weaker interface strip through the interface. Curves for models with uniform weak interfaces are also shown (dashed curves). (The weakest interface case is not shown for the weak slab on this figure because this is the model that exhibits very rapid slab break-off.) See also supplementary materials for videos of representative model runs with a low viscosity strip.

analysis by Conrad & Hager (1999), for example, as discussed by Behr & Becker (2018). However, our models show that the dynamic evolution of the slab introduces temporal changes in several parameters that can influence the dissipation balance such as slab

dip, shear zone width and the effect of power law creep on mantle viscosity.

To examine the extent to which the dynamic effects cause deviations from the dissipation analysis, we compare the convergence

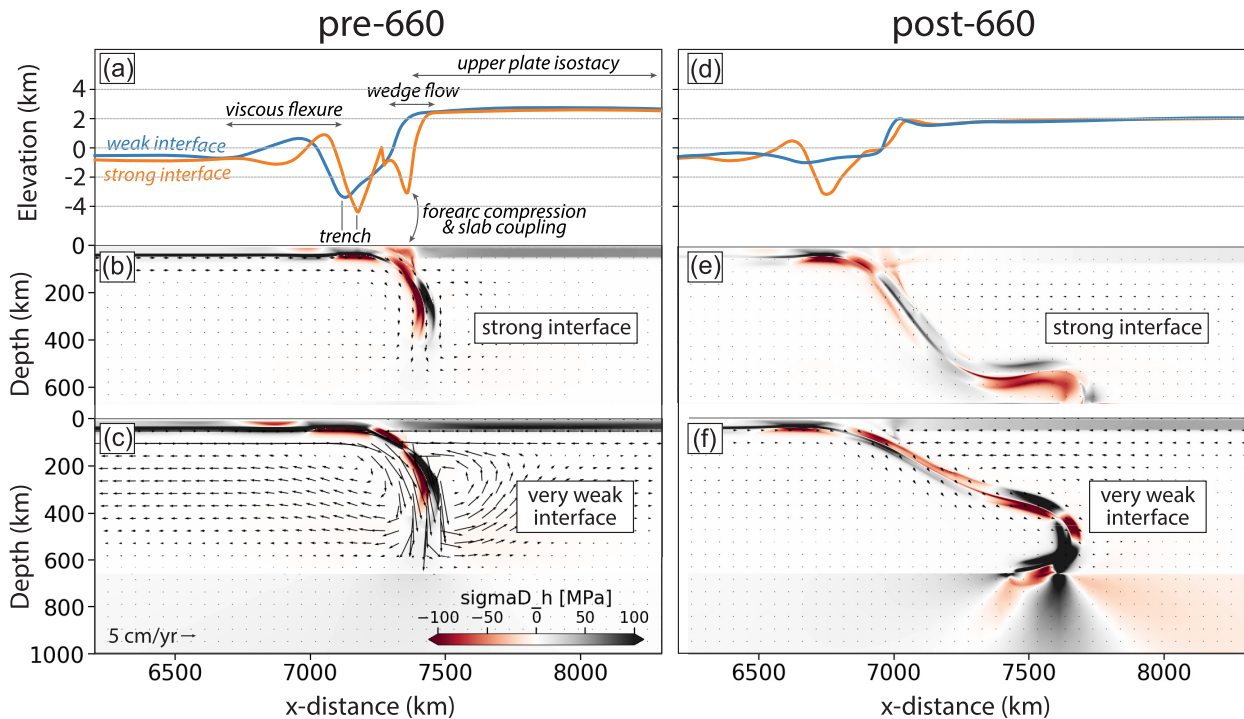


Figure 7. Spatial distribution of topography and horizontal deviatoric stress across the trench for two interface models (weak and strong) and the same slab strength (strong slab).

velocities computed in our models to those calculated using the Conrad & Hager (1999) energy balance formulation rewritten for a viscous shear zone and normalized slab and shear zone viscosities ($\eta'_l = \eta_l/\eta_m$, $\eta'_{sz} = \eta_{sz}/\eta_m$) as follows:

$$v_p = \frac{B}{\eta_m} \frac{C_s}{(C_\zeta + C_l \eta'_l r^{-3} + C_f \eta'_{sz} \zeta_f)}. \quad (8)$$

Here $B = \rho g \alpha \Delta T L_l h_l$, where ρ is the slab density, α is the thermal expansion coefficient, ΔT is the temperature difference from slab bottom to top, L_l is the slab length and h_l is the slab thickness. $C_\zeta = 3(\zeta + C_m)$, where ζ is the aspect ratio of mantle circulation (cell width/height), $r = R/h_l$ where R is the slab bending radius, ζ_f is the interface shear zone aspect ratio, and $C_{s,f,m,l}$ are fitting constants. Conrad & Hager (1999) chose $C_s = 1/\sqrt{\pi}$, for which they then found $C_l \approx 2.5$, $C_m \approx 2.5$ and $C_f \approx 1.2$ for their fixed geometry, 2-D computations. We compare the calculated velocities from this formulation to our observed model velocities for the post-660 model parameters for different slab strengths. The time step that we analyse is selected so that the trench is in a similar horizontal position between models (e.g. Figs 4b–d). The velocities from the dissipation analysis are calculated using the model input parameters, including the mantle reference viscosity, the initial radius of curvature of the slab, the initial slab thickness, the average slab strength and the starting shear zone aspect ratio.

Fig. 9(a) shows that the calculated V_c curves for these input parameters and the two end-member slab strengths generally bracket our model results, but they underestimate and overestimate convergence velocities for the strong and weak slab cases, respectively. Fig. 9(b) demonstrates, however, that a much better fit is produced if a larger radius of curvature and higher interface shear zone aspect ratio is assumed. This is consistent with the occurrence of rapid slab rollback, shallower slab dips and therefore a larger radius of curvature and a greater interface shear zone length in the weak interface

models (cf. Fig. 4). Fig. 9(b) thus illustrates that the dissipation analysis provides a good approximation of the effects of the interface on post-660, ‘steady-state’ convergence velocity for end-member slab strengths, particularly when these radius of curvature and shear zone geometry modifications are taken into account. However, the fastest convergence velocities, predicted by the dissipation analysis for very weak slabs and a very weak interface, are not realized in our dynamic models, as slab break-off occurs for these models prior the slab reaching the 660 (see also Section 4.4).

4.2 Interface viscosity and slab-660 interactions

The modelled effects of the interface on slab rollback and slab interactions with the 660-km-discontinuity is consistent with work by Čížková & Bina (2013). These authors showed that both plate and trench retreat rates increase with decreasing interface viscosity and relatedly, that stronger interfaces lead to steeper slab dips and more vertically oriented interactions between the slab and the 660. This effort and more recent work by Čížková & Bina (2019), along with our models (e.g. Fig. 2) show the important influence of the interface viscosity on the extent to which slabs penetrate the 660, with weak interfaces exhibiting such fast rollback that the slabs transiently lie flat on the transition zone or remain suspended in the upper mantle for significant periods of time. This is consistent with previous work demonstrating that slab stagnation is favoured by rapid slab rollback (Zhong & Gurnis 1995b; Christensen 1996; Čížková *et al.* 2002; Enns *et al.* 2005; Goes *et al.* 2017). Transient slab stagnation in the upper mantle may furthermore result from short-lengthscale variations in interface viscosity, such as those discussed in the low-viscosity-strip models in Section 3.3. However, for our models, the effect of the interface viscosity on slab-660 interactions are secondary to the effects of slab strength (cf. Davies 1995); for example Fig. 3 shows how the weak slab more easily penetrates the

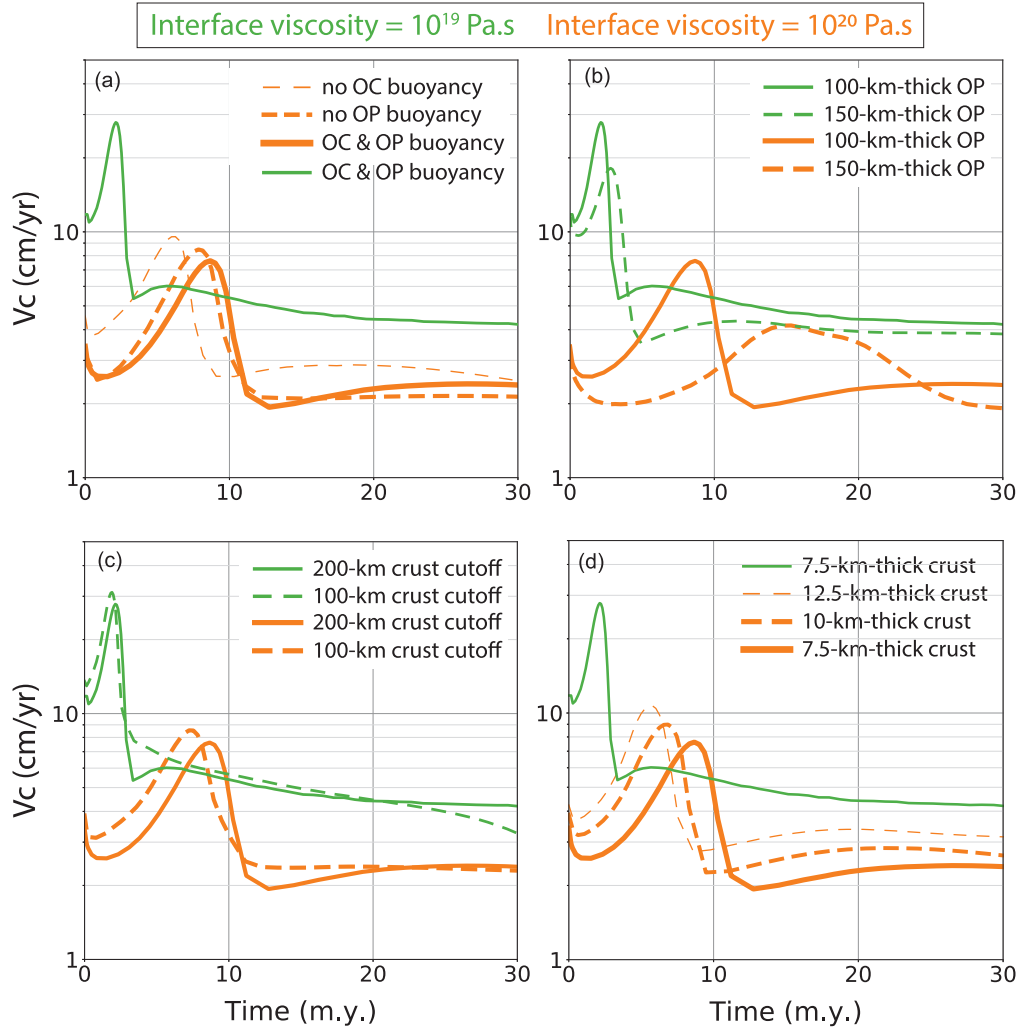


Figure 8. Comparison between effects on convergence velocity of changing (a) oceanic crust and upper plate density, (b) upper plate thickness, (c) crustal cut-off depth and (d) crustal thickness, relative to changing interface viscosity. All curves are for a single slab strength (Slab with core A, which is the strongest slab case). All three variations from the reference model produce visible effects, but they are much smaller in magnitude than the effects of changing interface viscosity. See Section 3.5 for further discussion.

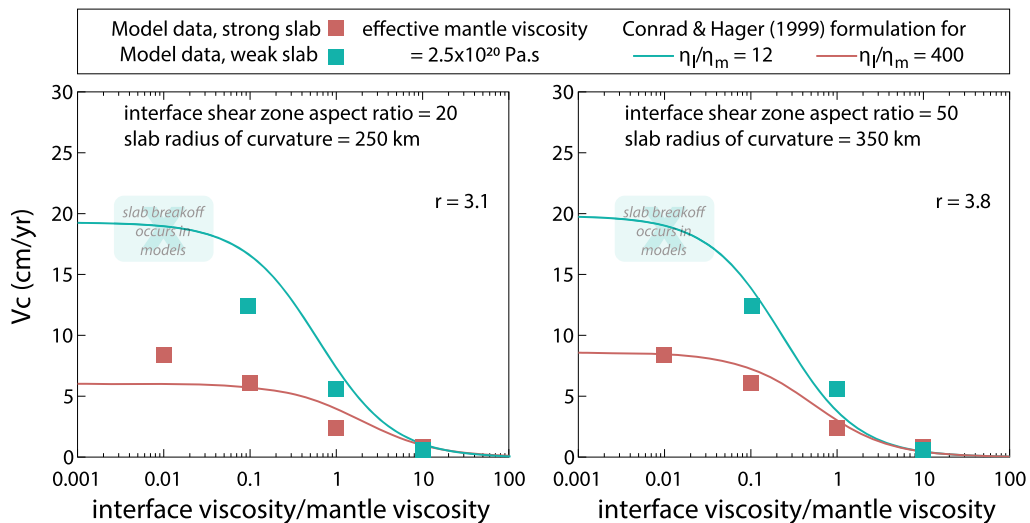


Figure 9. Comparison of computed convergence velocities as a function of interface viscosity from our dynamic subduction models (coloured squares) to the fixed geometry, energy balanced formulation of Conrad & Hager (1999) (coloured lines).

660 and exhibits a tighter buckling wavelength than the strong slab case, at constant interface viscosity.

4.3 Relationships between interface rheology and forearc topography

The relationships between interface rheology and forearc topography shown in Fig. 7 provide first-order estimates of stress orientation and topographic sign in the upper plate as a function of interface viscosity. For our simplified model set-up, a stronger interface leads to compressional stresses in the overriding plate forearc, but simultaneously leads to slightly reduced forearc topography due to strong coupling with the downgoing slab. A very weak interface, on the other hand, results in neutral to extensional stresses in the upper plate forearc and higher average topography landward of the trench. Similar results have been obtained in previous studies in which interface rheology is implemented as high versus low effective friction coefficients (e.g. Cattin *et al.* 1997; Hassani *et al.* 1997; Cerpa & Arcay 2020), whereas some studies have suggested the opposite relationship—that is high friction = high topography (e.g. Huang *et al.* 1997; Lamb & Davis 2003). Our use of free slip boundary conditions, and very simplified accretionary wedge and upper plate yielding dynamics, however, makes it difficult to test other potential feedback mechanisms that may be essential in influencing upper plate topographic development. For example, forearc compression may lead to uplift through thrust faulting and accretion and/or forearc underplating (Clift & Hartley 2007; Menant *et al.* 2020). Depending on material buoyancy, accreting/underplating may also serve to counteract the slab pull force (Keum & So 2021; Brizzi *et al.* 2021). On the other hand, lower shear stresses associated with the weak interface case could lead to normal faulting and potentially decreased topography and local forearc submergence (e.g. McIntosh *et al.* 1993; Cubas *et al.* 2013). The upper plate and trench topography will also be modulated by upper plate erosion and sediment delivery to the trench (e.g. Melnick & Echtler 2006); the sediment delivery process could itself feed back to influence interface viscosity. Future work that incorporates more realistic accretionary wedge dynamics, upper plate erosional processes and/or sediment delivery are thus essential to fully investigating the relationship between interface viscosity and topographic evolution.

4.4 Comparing model behaviours to observed subduction dynamics

For the range of slab strengths and background mantle viscosity implemented, our model results bracket the viscosity range for the subduction interface that will produce kinematics and behaviours that are consistent with modern plate tectonics (*cf.* King & Hager 1990; Conrad & Hager 1999). Convergence velocities in our models that broadly match modern subduction velocities are produced for the two intermediate interface viscosity cases (10^{19} – 10^{20} Pa s); this viscosity range is consistent with flow laws for quartz-rich sediments (closer to 10^{19} Pa s) or mixtures of sediments and mafic rocks (closer to 10^{20} Pa s, e.g. Tokle *et al.* 2019; Jin *et al.* 2001; Hirth & Kohlstedt 2004; Zhang *et al.* 2006; Behr & Becker 2018).

Models in which we implemented an interface viscosity of 10^{21} Pa s show overriding plate, subduction and convergence velocities that are extremely slow (Fig. 5). An interface viscosity this high would only be consistent with flow laws for cold, dry crustal rocks such as eclogite in the absence of any weakening mechanisms or mixing with weaker materials (Jin *et al.* 2001; Zhang *et al.* 2006).

All modern subduction zones show evidence for some sediment input (Plank & Langmuir 1993), so it is unlikely that any are governed entirely by the viscosity of mafic rocks, although this mechanism of subduction stalling could potentially have been important earlier in Earth's history prior to the evolution of felsic crust and associated weak sediments.

On the opposite end of the spectrum, models with both a weak slab and a weak interface lead to slab break-off. Slab break-off and tearing is a process for which there is evidence in the geological record (such as changes in magmatism, metamorphism and stress states, for example von Blanckenburg & Davies 1995; Atherton & Ghani 2002), and from seismological constraints (e.g. Hafkenscheid *et al.* 2006; Replumaz *et al.* 2010; Vargas & Mann 2013). Models show that slab break-off is favoured for weaker slabs, as expected, for example for a hotter mantle for early Earth (van Hunen & van den Berg 2008) and modifications of plate buoyancy, such as during the onset of continental collision (Davies & von Blanckenburg 1995; Baumann *et al.* 2010; van Hunen & Allen 2011; Duretz *et al.* 2011). Our results illustrate that changes in the viscosity of the interface in the presence of an already weak slab could also be a mechanism that promotes break-off due to pervasive yielding in the oceanic plate. The situation of a weak interface and a weak slab may not be physically unrealistic if considering, for example, the possible role of serpentinization. Serpentine mineral viscosities are predicted to be exceptionally low based on laboratory experiments (Escartin *et al.* 2001; Hilairt *et al.* 2007). Thus, potential candidate slabs for unstable subduction and slab break-off facilitated by weak-interface-induced-rollback could include, for example, young slabs that exhibit deep hydrothermal circulation that both serpentinizes the slab itself, and produces sufficient fluids during subduction dehydration to also strongly serpentinize the mantle wedge directly above the slab.

4.5 Implications for short-timescale plate velocity changes

Our low viscosity crustal strip models discussed in Section 3.3 have implications for the mechanisms that can lead to relatively short (~ 10 Myr) timescale or pulse-like accelerations and decelerations in plate convergence or trench retreat rates. Such changes in relative plate motions are recorded for several subduction systems throughout Earth's history (e.g. Tebbens & Cande 1997; Torsvik *et al.* 2010; Doubrovine *et al.* 2012) and have been attributed to a wide range of geodynamic processes, such as plume-head arrival (van Hinsbergen *et al.* 2011; Cande & Stegman 2011), double subduction (Jagoutz *et al.* 2015; Holt *et al.* 2017), a combination of the two (Pusok & Stegman 2020), slab interactions at the 660 (Zhong & Gurnis 1995b; Goes *et al.* 2008), upper plate orogenic growth (Iaffaldano *et al.* 2006; Meade & Conrad 2008) or transitions from oceanic to continental lithosphere and the onset of continental collision (e.g. Capitanio *et al.* 2010), among others.

Our results in Fig. 6 support the hypothesis that changes in the strength of subducting crustal material occupying the interface is an additional potential mechanism of increasing or decreasing convergence velocities (*cf.* Behr & Becker 2018). The weak slab case in particular suggests that a decrease in interface viscosity of one order of magnitude could lead to a factor of two increase in the convergence velocity, with acceleration rates that scale with the initial convergence rate as $dV_c/dt \approx 0.1V_c$ Myr. Unlike some of the other suggested mechanisms, interface control as discussed here involves a potential and explicit coupling between surface processes and dynamics through sediment transport. Interface control for plate

velocity changes may be especially relevant to subduction systems in which the sediment supply and composition of the downgoing oceanic or hyperextended continental plate is highly variable in the convergence direction, such as the Alpine-Tethys and current Mediterranean subduction systems, and/or to time periods in Earth's history where oscillations in trench sedimentation were generated (e.g. glaciation/deglaciation events).

The sediment-strip models for the strong slab model cases exhibit a more modest change in convergence rates of less than a factor of two; however, these models are still associated with a punctuated pulse of slab rollback with trench retreat rates that can be a factor of two larger than the reference constant-viscosity slab case. Thus, even for constant convergence rate subduction systems, punctuated stages of trench retreat may occur as a result of variations in subducted crustal inputs. Moreover, if trench and convergence kinematics changes can be documented independently, the phase shift between the transient responses for strong and weak slabs as seen in Fig. 6 can provide an indirect constraint on effective slab rheology.

5 CONCLUSIONS

We explored the role of the plate interface in influencing the kinematics and dynamics of an upper-mantle-scale subduction system. Our results confirm that interface viscosity can strongly influence convergence velocities both prior to and after slab interaction with a viscosity increase at the 660-km-discontinuity. Our dynamically consistent models are broadly consistent with simplified viscous dissipation analysis; however, some deviations occur due to changes in slab geometry which affects both the slab bending radius and the aspect ratio of the interface shear zone. Substantiating previous work, we show that both subducting plate velocities and trench retreat rates increase with decreasing interface viscosity, and relatedly, that stronger interfaces lead to steeper slab dips, more vertical sinking and hence reduced slab flattening on the 660. We also explore the relationship between interface rheology and forearc topography: a stronger interface leads to compressional deviatoric stresses in the overriding plate and reduced forearc topography, whereas a weaker interface results in neutral to extensional stresses in the forearc and higher forearc topography. We also tested the response of the subduction system to transient perturbation of interface viscosity, intended to model changes in lithological inputs on the subducting plate, such as patches of weak sedimentary cover or serpentinitized oceanic mantle lithosphere. These models demonstrate that lithological variations can lead to ~ 10 Myr timescale, pulse-like accelerations and decelerations in convergence and trench retreat rates. The modelled transients are similar in duration and magnitude to those documented in the geological record, and how the perturbation is partitioned kinematically depends on slab strength in diagnostic ways. Our work substantiates previous suggestions that there is an important link between large-scale subduction dynamics and the material inputs and geological history of the downgoing plate, indicating avenues to further understand subduction systems dynamics from integrated geological–geophysical analysis.

ACKNOWLEDGMENTS

The authors acknowledge thoughtful reviews from Nestor Cerpa and Mike Gurnis that led to improvements of this manuscript. This work was supported by a European Research Council (ERC) Starting Grant (947659) awarded to WMB. AFH was supported by NSF EAR 2119842 and TWB was supported by NSF EAR 1925939

and 1853856. The computations of this work used the Extreme Science and Engineering Discovery Environment (XSEDE), supported by NSF Grant No. ACI-15485x62. The authors also thank the Computational Infrastructure for Geodynamics (geodynamics.org), which is funded by the NSF under awards EAR-0949446 and EAR-1550901, for supporting the development of ASPECT. CF acknowledges support from Dipartimento di Eccellenza, Roma Tre. All model images utilized the perceptually uniform colourmaps from Crameri (2018).

DATA AVAILABILITY

All files needed to run the models presented here are accessible via the ETH Research Collection at doi:10.3929/ethz-b-000533201.

REFERENCES

- Abercrombie, R.E., Antolik, M., Felzer, K. & Ekström, G., 2001. The 1994 Java tsunami earthquake: slip over a subducting seamount, *J. geophys. Res.*, **106**(B4), 6595–6607.
- Agard, P., Plunder, A., Angiboust, S., Bonnet, G. & Ruh, J., 2018. The subduction plate interface: rock record and mechanical coupling (from long to short timescales), *Lithos*, **320–321**, 537–566.
- Androvičová, A., Čížková, H. & van den Berg, A., 2013. The effects of rheological decoupling on slab deformation in the Earth's upper mantle, *Stud. Geophys. Geod.*, **57**(3), 460–481.
- Angiboust, S., Agard, P., Raimbourg, H., Yamato, P. & Huet, B., 2011. Subduction interface processes recorded by eclogite-facies shear zones (Monviso, W. Alps), *Lithos*, **127**, 222–238.
- Atherton, M. & Ghani, A., 2002. Slab breakoff: a model for Caledonian, Late Granite syn-collisional magmatism in the orthotectonic (metamorphic) zone of Scotland and Donegal, Ireland, *Lithos*, **62**(3–4), 65–85.
- Audet, P. & Schaeffer, A.J., 2018. Fluid pressure and shear zone development over the locked to slow slip region in Cascadia, *Sci. Adv.*, **4**(3), eaar2982, doi:10.1126/sciadv.aar2982.
- Bangerth, W., et al., 2018. *ASPECT: Advanced Solver for Problems in Earth's ConvecTion, User Manual*, figshare. Journal contribution. <https://doi.org/10.6084/m9.figshare.4865333.v7>.
- Barnes, P.M. et al., 2020. Slow slip source characterized by lithological and geometric heterogeneity, *Sci. Adv.*, **6**(13), eaay3314, doi:10.1126/sciadv.aay3314.
- Bassett, D. & Watts, A.B., 2015. Gravity anomalies, crustal structure, and seismicity at subduction zones: 2. Interrelationships between fore-arc structure and seismogenic behavior, *Geochem., Geophys., Geosyst.*, **16**, 1541–1576.
- Baumann, C., Gerya, T.V. & Connolly, J.A., 2010. Numerical modelling of spontaneous slab breakoff dynamics during continental collision, *Geol. Soc., Lond., Spec. Publ.*, **332**(1), 99–114.
- Bebout, G.E., 2013. Chemical and isotopic cycling in subduction zones, in *Treatise on Geochemistry*, 2nd edn, pp. 703–747, Elsevier Inc.
- Becker, T.W. & Faccenna, C., 2009. A review of the role of subduction dynamics for regional and global plate motions, in *Subduction Zone Geodynamics*, pp. 3–34, eds Fuciniello, F. & Lallemand, S., Springer.
- Behr, W.M. & Becker, T.W., 2018. Sediment control on subduction plate speeds, *Earth planet. Sci. Lett.*, **502**, 166–173.
- Billen, M.I., 2008. Modeling the dynamics of subducting slabs, *Ann. Rev. Earth planet. Sci.*, **36**, 325–356.
- Billen, M.I. & Gurnis, M., 2001. A low viscosity wedge in subduction zones, *Earth planet. Sci. Lett.*, **193**(1–2), 227–236.
- Billen, M.I. & Gurnis, M., 2005. Constraints on subducting plate strength within the Kermadec trench, *J. geophys. Res.*, **110**, doi:10.1029/2004JB003308.
- Billen, M.I. & Hirth, G., 2005. Newtonian versus non-Newtonian upper mantle viscosity: implications for subduction initiation, *Geophys. Res. Lett.*, **32**, doi:10.1029/2005GL023457.

- Boulton, C., Niemeijer, A.R., Hollis, C.J., Townend, J., Raven, M.D., Kulhanek, D.K. & Shepherd, C.L., 2019. Temperature-dependent frictional properties of heterogeneous Hikurangi subduction zone input sediments, ODP Site 1124, *Tectonophysics*, **757**, 123–139.
- Braden, Z. & Behr, W., 2021. Weakening mechanisms in a basalt-hosted subduction megathrust fault segment, southern Alaska, *J. geophys. Res.*, **126**(9), doi:10.1029/2021JB022039.
- Brizzi, S., Becker, T.W., Faccenna, C., Behr, W.M., van Zelst, I., Dal Zilio, L. & van Dinther, Y., 2021. The role of sediment subduction and buoyancy on subduction dynamics and geometry, *Geophys. Res. Lett.*, **48**(20), doi:10.1029/2021GL096266.
- Buffett, B. & Becker, T.W., 2012. Bending stress and dissipation in subducted lithosphere, *J. geophys. Res.*, **117**(B5), doi:10.1029/2012JB009205.
- Burov, E. et al., 2014. Rheological and geodynamic controls on the mechanisms of subduction and HP/UHP exhumation of crustal rocks during continental collision: insights from numerical models, *Tectonophysics*, **631**, 212–250.
- Calvert, A.J., Bostock, M.G., Savard, G. & Unsworth, M.J., 2020. Cascadia low frequency earthquakes at the base of an overpressured subduction shear zone, *Nat. Commun.*, **11**(1), 1–10.
- Cande, S.C. & Stegman, D.R., 2011. Indian and African plate motions driven by the push force of the Reunion plume head, *Nature*, **475**(7354), 47–52.
- Capitanio, F.A., Morra, G. & Goes, S., 2007. Dynamic models of downgoing plate-buoyancy driven subduction: subduction motions and energy dissipation, *Earth planet. Sci. Lett.*, **262**, 284–297.
- Capitanio, F.A., Morra, G., Goes, S., Weinberg, R.F. & Moresi, L., 2010. India-Asia convergence driven by the subduction of the Greater Indian continent, *Nat. Geosci.*, **3**, 136–139.
- Cattin, R., Lyon-Caen, H. & Chéry, J., 1997. Quantification of interplate coupling in subduction zones and forearc topography, *Geophys. Res. Lett.*, **24**(13), 1563–1566.
- Cerpa, N.G. & Arcay, D., 2020. Overriding plate velocity control on surface topography in 2-D models of subduction zones, *Geochem. Geophys. Geosyst.*, **21**(4), e2019GC008900.
- Chen, G., Cheng, Q., Peters, S.E., Spencer, C.J. & Zhao, M., 2022. Feedback between surface and deep processes: insight from time series analysis of sedimentary record, *Earth planet. Sci. Lett.*, **579**, doi:10.1016/j.epsl.2021.117352.
- Chen, Z., Schellart, W.P., Duarte, J.C. & Strak, V., 2017. Topography of the overriding plate during progressive subduction: a dynamic model to explain forearc subsidence, *Geophys. Res. Lett.*, **44**(19), 9632–9643.
- Christensen, U.R., 1996. The influence of trench migration on slab penetration into the lower mantle, *Earth planet. Sci. Lett.*, **140**(1–4), 27–39.
- Čížková, H. & Bina, C.R., 2013. Effects of mantle and subduction-interface rheologies on slab stagnation and trench rollback, *Earth planet. Sci. Lett.*, **379**, 95–103.
- čížková, H. & Bina, C.R., 2019. Linked influences on slab stagnation: interplay between lower mantle viscosity structure, phase transitions, and plate coupling, *Earth planet. Sci. Lett.*, **509**, 88–99.
- Čížková, H., van Hunen, J., van den Berg, A.P. & Vlaar, N.J., 2002. The influence of rheological weakening and yield stress on the interaction of slabs with the 670 km discontinuity, *Earth planet. Sci. Lett.*, **199**(3–4), 447–457.
- Clarke, A.P., Vannucchi, P. & Morgan, J., 2018. Seamount chain–subduction zone interactions: implications for accretionary and erosive subduction zone behavior, *Geology*, **46**(4), 367–370.
- Clift, P., 2017. A revised budget for Cenozoic sedimentary carbon subduction, *Rev. Geophys.*, **55**(1), 97–125.
- Clift, P.D. & Hartley, A.J., 2007. Slow rates of subduction erosion and coastal underplating along the Andean margin of Chile and Peru, *Geology*, **35**(6), 503–506.
- Cloos, M., 1985. Thermal evolution of convergent plate margins: thermal modeling and reevaluation of isotopic Ar-ages for blueschists in the Franciscan Complex of California, *Tectonics*, **4**(5), 421–433.
- Cloos, M., 1992. Thrust-type subduction-zone earthquakes and seamount asperities: a physical model for seismic rupture, *Geology*, **20**(7), 601–604.
- Cloos, M., 1993. Lithospheric buoyancy and collisional orogenesis: subduction of oceanic plateaus, continental margins, island arcs, spreading ridges, and seamounts, *Bull. geol. Soc. Am.*, **105**(6), 715.
- Conrad, C.P. & Hager, B.H., 1999. Effects of plate bending and fault strength at subduction zones on plate dynamics, *J. geophys. Res.*, **104**(B8), 17 551–17 571.
- Cramer, F., 2018. Geodynamic diagnostics, scientific visualisation and staglab 3.0, *Geosci. Model Dev.*, **11**(6), 2541–2562.
- Cramer, F., Lithgow-Bertelloni, C. & Tackley, P.J., 2017. The dynamical control of subduction parameters on surface topography, *Geochem. Geophys. Geosyst.*, **18**(4), 1661–1687.
- Cubas, N., Avouac, J.-P., Leroy, Y.M. & Pons, A., 2013. Low friction along the high slip patch of the 2011 Mw 9.0 Tohoku-Oki earthquake required from the wedge structure and extensional splay faults, *Geophys. Res. Lett.*, **40**(16), 4231–4237.
- Davies, G.F., 1995. Penetration of plates and plumes through the mantle transition zone, *Earth planet. Sci. Lett.*, **133**, 507–516.
- Davies, J.H. & von Blanckenburg, F., 1995. Slab breakoff: a model of lithosphere detachment and its test in the magmatism and deformation of collisional orogens, *Earth planet. Sci. Lett.*, **129**(1–4), 85–102.
- Delph, J.R., Thomas, A.M. & Levander, A., 2021. Subcretionary tectonics: linking variability in the expression of subduction along the Cascadia forearc, *Earth planet. Sci. Lett.*, **556**, 116724.
- Dobrovine, P.V., Steinberger, B. & Torsvik, T.H., 2012. Absolute plate motions in a reference frame defined by moving hot spots in the Pacific, Atlantic, and Indian oceans, *J. geophys. Res.*, **117**(B9), doi:10.1029/2011JB009072.
- Duret, T., Gerya, T.V. & May, D.A., 2011. Numerical modelling of spontaneous slab breakoff and subsequent topographic response, *Tectonophysics*, **502**(1–2), 244–256.
- Enns, A., Becker, T.W. & Schmeling, H., 2005. The dynamics of subduction and trench migration for viscosity stratification, *Geophys. J. Int.*, **160**(2), 761–775.
- Escartin, J., Hirth, G. & Evans, B., 2001. Strength of slightly serpentinized peridotites: implications for the tectonics of oceanic lithosphere, *Geology*, **29**(11), 1023–1026.
- Fagereng, Å. & Sibson, R.H., 2010. Mélange rheology and seismic style, *Geology*, **38**(8), 751–754.
- Foley, S., Tiepolo, M. & Vannucci, R., 2002. Growth of early continental crust controlled by melting of amphibolite in subduction zones, *Nature*, **417**(6891), 837–840.
- Funiciello, F., Faccenna, C., Heuret, A., Di Giuseppe, E., Lallemand, S. & Becker, T.W., 2008. Trench migration, net rotation and slab-mantle coupling, *Earth planet. Sci. Lett.*, **271**, 233–240.
- Furukawa, Y., 1993. Depth of the decoupling plate interface and thermal structure under arcs, *J. geophys. Res.*, **98**(B11), 20 005–20 013.
- Garel, F., Goes, S., Davies, D.R., Davies, J.H., Kramer, S.C. & Wilson, C.R., 2014. Interaction of subducted slabs with the mantle transition zone: a regime diagram from 2-D thermo-mechanical models with a mobile trench and an overriding plate, *Geochem., Geophys., Geosyst.*, **15**, doi:10.1002/2014GC005257.
- Gerya, T.V., Stöckhert, B. & Perchuk, A.L., 2002. Exhumation of high-pressure metamorphic rocks in a subduction channel: a numerical simulation, *Tectonics*, **21**(6), 6–1.
- Goes, S., Capitanio, F.A. & Morra, G., 2008. Evidence of lower-mantle slab penetration phases in plate motions, *Nature*, **451**(7181), 981–984.
- Goes, S., Agrusta, R., van Hunen, J. & Garel, F., 2017. Subduction-transition zone interaction: a review, *Geosphere*, **13**(3), 644–664.
- Grigull, S., Krohe, A., Moos, C., Wassmann, S. & Stöckhert, B., 2012. ‘Order from chaos’: a field-based estimate on bulk rheology of tectonic mélanges formed in subduction zones, *Tectonophysics*, **568**, 86–101.
- Guillot, S., Schwartz, S., Reynard, B., Agard, P. & Prigent, C., 2015. Tectonic significance of serpentinites, *Tectonophysics*, **646**, 1–19.
- Gulick, S.P. et al., 2011. Updip rupture of the 2004 Sumatra earthquake extended by thick indurated sediments, *Nat. Commun.*, **4**(7), 453–456.
- Hafkenschied, E., Wortel, M.J.R. & Spakman, W., 2006. Subduction history of the Tethyan region derived from seismic tomography and tectonic reconstructions, *J. geophys. Res.*, **111**(B8), doi:10.1029/2005JB003791.

- Hager, B.H., 1984. Subducted slabs and the geoid: constraints on mantle rheology and flow, *J. geophys. Res.*, **89**, 6003–6015.
- Han, S., Bangs, N.L., Carbotte, S.M., Saffer, D.M. & Gibson, J.C., 2017. Links between sediment consolidation and Cascadia megathrust slip behaviour, *Nat. Geosci.*, **10**, 954–959.
- Hassani, R., Jongmans, D. & Chéry, J., 1997. Study of plate deformation and stress in subduction processes using two-dimensional numerical models, *J. geophys. Res.*, **102**(B8), 17 951–17 965.
- Heister, T., Dannberg, J., Gasmöller, R. & Bangerth, W., 2017. High accuracy mantle convection simulation through modern numerical methods—II: realistic models and problems, *Geophys. J. Int.*, **210**, 833–851.
- Heuret, A., Conrad, C., Funicello, F., Lallemand, S. & Sandri, L., 2012. Relation between subduction megathrust earthquakes, trench sediment thickness and upper plate strain, *Geophys. Res. Lett.*, **39**(5), doi:10.1029/2011GL050712.
- Hilairt, N., Reynard, B., Wang, Y., Daniel, I., Merkel, S., Nishiyama, N. & Petitgirard, S., 2007. High-pressure creep of serpentine, interseismic deformation, and initiation of subduction, *Science*, **318**(5858), 1910–1913.
- Hirth, G. & Kohlstedt, D.L., 2004. Rheology of the upper mantle and the mantle wedge: a view from the experimentalists, in *Inside the Subduction Factory*, Vol. 138 of Geophys. Monograph, pp. 83–105, ed. Eiler, J., American Geophysical Union.
- Hirth, G., Teyssier, C. & Dunlap, J.W., 2001. An evaluation of quartzite flow laws based on comparisons between experimentally and naturally deformed rocks, *Int. J. Earth Sci.*, **90**(1), 77–87.
- Holt, A., Royden, L. & Becker, T., 2017. The dynamics of double slab subduction, *Geophys. J. Int.*, **209**(1), 250–265.
- Holt, A.F. & Becker, T.W., 2016. The effect of a power-law mantle viscosity on trench retreat rate, *Geophys. J. Int.*, **208**, 491–507.
- Holt, A.F. & Condit, C.B., 2021. Slab temperature evolution over the lifetime of a subduction zone, *Geochem., Geophys., Geosyst.*, **22**(6), e2020GC009476, doi:10.1029/2020GC009476.
- Holt, A.F., Becker, T.W. & Buffett, B.A., 2015. Trench migration and overriding plate stress in dynamic subduction models, *Geophys. J. Int.*, **201**, 172–192.
- Holt, W.E., 1995. Flow fields within the Tonga slab determined from the moment tensors of deep earthquakes, *Geophys. Res. Lett.*, **22**, 989–992.
- Huang, S., Sacks, I. & Snoke, J., 1997. Topographic and seismic effects of long-term coupling between the subducting and overriding plates beneath Northeast Japan, *Tectonophysics*, **269**(3–4), 279–297.
- Iaffaldano, G., Bunge, H.-P. & Dixon, T.H., 2006. Feedback between mountain belt growth and plate convergence, *Geology*, **34**, 893–896.
- Jagoutz, O., Royden, L., Holt, A.F. & Becker, T.W., 2015. Anomalously fast convergence of India and Eurasia caused by double subduction, *Nat. Commun.*, **8**(6), 475–478.
- Jin, Z.-M., Zhang, J., Green, H. & Jin, S., 2001. Eclogite rheology: implications for subducted lithosphere, *Geology*, **29**(8), 667–670.
- Kerrick, D.M. & Connolly, J. A.D., 2001. Metamorphic devolatilization of subducted marine sediments and the transport of volatiles into the Earth's mantle, *Nature*, **411**, 293–296.
- Keum, J.-Y. & So, B.-D., 2021. Effect of buoyant sediment overlying subducting plates on trench geometry: 3D viscoelastic free subduction modeling, *Geophys. Res. Lett.*, **48**(9), e2021GL093498.
- Kincaid, C. & Sacks, I.S., 1997. Thermal and dynamical evolution of the upper mantle in subduction zones, *J. geophys. Res.*, **102**, 12 295–12 315.
- King, S.D. & Hager, B.H., 1990. The relationship between plate velocity and trench viscosity in Newtonian and power-law subduction calculations, *Geophys. Res. Lett.*, **17**, 2409–2412.
- King, S.D. & Masters, G., 1992. An inversion for radial viscosity structure using seismic tomography, *Geophys. Res. Lett.*, **19**, 1551–1554.
- Kitamura, Y. & Kimura, G., 2012. Dynamic role of tectonic Mélange during interseismic process of plate boundary mega earthquakes, *Tectonophysics*, **568**, 39–52.
- Kotowski, A.J. & Behr, W.M., 2019. Length scales and types of heterogeneities along the deep subduction interface: insights from exhumed rocks on Syros Island, Greece, *Geosphere*, **15**(4), 1038–1065.
- Kronbichler, M., Heister, T. & Bangerth, W., 2012. High accuracy mantle convection simulation through modern numerical methods, *Geophys. J. Int.*, **191**, 12–29.
- Kurzawski, R.M., Niemeijer, A.R., Stipp, M., Charpentier, D., Behrmann, J.H. & Spiers, C.J., 2018. Frictional properties of subduction input sediments at an erosive convergent continental margin and related controls on décollement slip modes: the Costa Rica Seismogenesis Project, *J. geophys. Res.*, **123**(10), 8385–8408.
- Lamb, S. & Davis, P., 2003. Cenozoic climate change as a possible cause for the rise of the Andes, *Nature*, **425**, 792–797.
- Laursen, J., Scholl, D.W. & von Huene, R., 2002. Neotectonic deformation of the central Chile margin: deepwater forearc basin formation in response to hot spot ridge and seamount subduction, *Tectonics*, **21**(5), 2–1.
- McIntosh, K., Silver, E. & Shipley, T., 1993. Evidence and mechanisms for forearc extension at the accretionary Costa Rica convergent margin, *Tectonics*, **12**(6), 1380–1392.
- Meade, B.J. & Conrad, C.P., 2008. Andean growth and the deceleration of South American subduction: time evolution of a coupled orogen-subduction system, *Earth planet. Sci. Lett.*, **275**(1–2), 93–101.
- Melnick, D. & Echter, H.P., 2006. Inversion of forearc basins in south-central Chile caused by rapid glacial age trench fill, *Geology*, **34**(9), 709–712.
- Menant, A., Angiboust, S., Gerya, T., Lacassin, R., Simoes, M. & Grandin, R., 2020. Transient stripping of subducting slabs controls periodic forearc uplift, *Nat. Commun.*, **11**(1), 1–10.
- Minshull, T.A., 2009. Geophysical characterisation of the ocean–continent transition at magma-poor rifted margins, *C. R. Geosci.*, **341**(5), 382–393.
- Moresi, L. & Solomatov, V., 1998. Mantle convection with a brittle lithosphere: thoughts on the global tectonic styles of the Earth and Venus, *Geophys. J. Int.*, **133**, 669–682.
- Nedimović, M.R., Hyndman, R.D., Ramachandran, K. & Spence, G.D., 2003. Reflection signature of seismic and aseismic slip on the northern Cascadia subduction interface, *Nature*, **424**(6947), 416–420.
- Phillips, N.J., Belzer, B., French, M.E., Rowe, C.D. & Ujiie, K., 2020. Frictional strengths of subduction thrust rocks in the region of shallow slow earthquakes, *J. geophys. Res.*, **125**(3), e2019JB018888.
- Plank, T. & Langmuir, C.H., 1993. Tracing trace elements from sediment input to volcanic output at subduction zones, *Nature*, **362**(6422), 739–743.
- Pokorný, J., čížková, H. & van den Berg, A., 2021. Feedbacks between subduction dynamics and slab deformation: combined effects of nonlinear rheology of a weak decoupling layer and phase transitions, *Phys. Earth Planet. Inter.*, **313**, doi:10.1016/j.pepi.2021.106679.
- Pusok, A.E. & Stegman, D.R., 2020. The convergence history of India-Eurasia records multiple subduction dynamics processes, *Sci. Adv.*, **6**(19), doi:10.1126/sciadv.aaz8681.
- Ratnaswamy, V., Stadler, G. & Gurnis, M., 2015. Adjoint-based estimation of plate coupling in a non-linear mantle flow model: theory and examples, *Geophys. J. Int.*, **202**(2), 768–786.
- Rea, D.K. & Ruff, L.J., 1996. Composition and mass flux of sediment entering the world's subduction zones: implications for global sediment budgets, great earthquakes, and volcanism, *Earth planet. Sci. Lett.*, **140**(1–4), 1–12.
- Replumaz, A., Negredo, A.M., Guillot, S. & Villaseñor, A., 2010. Multiple episodes of continental subduction during India/Asia convergence: insight from seismic tomography and tectonic reconstruction, *Tectonophysics*, **483**, 125–134.
- Ribe, N.M., Stutzmann, E., Ren, Y. & Van Der Hilst, R., 2007. Buckling instabilities of subducted lithosphere beneath the transition zone, *Earth planet. Sci. Lett.*, **254**(1–2), 173–179.
- Ricard, Y., Richards, M.A., Lithgow-Bertelloni, C. & Le Stunff, Y., 1993. A geodynamic model of mantle density heterogeneity, *J. geophys. Res.*, **98**, 21 895–21 909.
- Scholz, C.H. & Small, C., 1997. The effect of seamount subduction on seismic coupling, *Geology*, **25**(6), 487–490.
- Seyler, C., Kirkpatrick, J., Savage, H., Hirose, T. & Faulkner, D., 2020. Rupture to the trench? Frictional properties and fracture energy of incoming sediments at the Cascadia subduction zone, *Earth planet. Sci. Lett.*, **546**, doi:10.1016/j.epsl.2020.116413.

- Sobolev, S.V. & Brown, M., 2019. Surface erosion events controlled the evolution of plate tectonics on earth, *Nature*, **570**(7759), 52–57.
- Stegman, D.R., Freeman, J., Schellart, W.P., Moresi, L. & May, D., 2006. Influence of trench width on subduction hinge retreat rates in 3-D models of slab rollback, *Geochem. Geophys. Geosyst.*, **7**(3), doi:10.1029/2005GC001056.
- Stöckhert, B., Wachmann, M., Küster, M. & Bimmermann, S., 1999. Low effective viscosity during high pressure metamorphism due to dissolution precipitation creep: the record of HP–LT metamorphic carbonates and siliciclastic rocks from Crete, *Tectonophysics*, **303**(1–4), 299–319.
- Tebbens, S. & Cande, S., 1997. Southeast Pacific tectonic evolution from early Oligocene to present, *J. geophys. Res.*, **102**(B6), 12 061–12 084.
- Tewksbury-Christle, C., Behr, W. & Helper, M., 2021. Tracking deep sediment underplating in a fossil subduction margin: implications for interface rheology and mass and volatile recycling, *Geochem., Geophys., Geosyst.*, **22**, e2020GC009463.
- Tewksbury-Christle, C.M. & Behr, W.M., 2021. Constraints from exhumed rocks on the seismic signature of the deep subduction interface, *Geophys. Res. Lett.*, **48**(18), doi:10.1029/2021GL093831.
- Tobin, H.J. & Saffer, D.M., 2009. Elevated fluid pressure and extreme mechanical weakness of a plate boundary thrust, Nankai trough subduction zone, *Geology*, **37**(8), 679–682.
- Tokle, L., Hirth, G. & Behr, W.M., 2019. Flow laws and fabric transitions in wet quartzite, *Earth planet. Sci. Lett.*, **505**, 152–161.
- Torsvik, T.H., Steinberger, B., Gurnis, M. & Gaina, C., 2010. Plate tectonics and net lithosphere rotation over the past 150 My, *Earth planet. Sci. Lett.*, **291**(1–4), 106–112.
- van Hinsbergen, D.J., Steinberger, B., Doubrovine, P.V. & Gassmüller, R., 2011. Acceleration and deceleration of India-Asia convergence since the Cretaceous: roles of mantle plumes and continental collision, *J. geophys. Res.*, **116**(B6), doi:10.1029/2010JB008051.
- van Hunen, J. & Allen, M.B., 2011. Continental collision and slab break-off: a comparison of 3-D numerical models with observations, *Earth planet. Sci. Lett.*, **302**(1–2), 27–37.
- van Hunen, J. & van den Berg, A.P., 2008. Plate tectonics on the early Earth: limitations imposed by strength and buoyancy of subducted lithosphere, *Lithos*, **103**, 217–235.
- Vargas, C.A. & Mann, P., 2013. Tearing and breaking off of subducted slabs as the result of collision of the Panama Arc-Indenter with northwestern South America, *Bull. seism. Soc. Am.*, **103**, 2025–2046.
- von Blanckenburg, F. & Davies, J.H., 1995. Slab breakoff: a model for syncollisional magmatism and tectonics in the alps, *Tectonics*, **14**(1), 120–131.
- Von Huene, R. & Scholl, D.W., 1991. Observations at convergent margins concerning sediment subduction, subduction erosion, and the growth of continental crust, *Rev. Geophys.*, **29**(3), 279–316.
- Vrolijk, P., 1990. On the mechanical role of smectite in subduction zones, *Geology*, **18**(8), 703–707.
- Wada, I. & Wang, K., 2009. Common depth of slab-mantle decoupling: reconciling diversity and uniformity of subduction zones, *Geochem. Geophys. Geosyst.*, **10**(10), doi:10.1029/2009GC002570.
- Wada, I., Wang, K., He, J. & Hyndman, R.D., 2008. Weakening of the subduction interface and its effects on surface heat flow, slab dehydration, and mantle wedge serpentinization, *J. geophys. Res.*, **113**(B4), doi:10.1029/2007JB005190.
- Wu, B., Conrad, C.P., Heuret, A., Lithgow-Bertelloni, C. & Lallemand, S., 2008. Reconciling strong slab pull and weak plate bending: the plate motion constraint on the strength of mantle slabs, *Earth planet. Sci. Lett.*, **272**, 412–421.
- Zhang, J., Green II, H.W. & Bozhilov, K.N., 2006. Rheology of omphacite at high temperature and pressure and significance of its lattice preferred orientations, *Earth planet. Sci. Lett.*, **246**(3–4), 432–443.
- Zhong, S. & Gurnis, M., 1994. Controls on trench topography from dynamic models of subducted slabs, *J. geophys. Res.*, **99**(B8), 15 683–15 695.
- Zhong, S. & Gurnis, M., 1995a. Towards a realistic simulation of plate margins in mantle convection, *Geophys. Res. Lett.*, **22**(8), 981–984.
- Zhong, S. & Gurnis, M., 1995b. Mantle convection with plates and mobile, faulted plate margins, *Science*, **267**, 838–842.

SUPPORTING INFORMATION

Supplementary data are available at *GJI* online.

supplementary_movies.zip

Please note: Oxford University Press is not responsible for the content or functionality of any supporting materials supplied by the authors. Any queries (other than missing material) should be directed to the corresponding author for the paper.